Generation of Graphite Particles by Abrasion and Their Characterization

A Dissertation Presented to

The Faculty of the Graduate School

At the University of Missouri

In Partial Fulfillment

Of the Requirements for the Degree

Doctor of Philosophy

By

RAYMOND STEVEN TROY

Drs. Robert V. Tompson, Tushar K. Ghosh, Sudarshan K. Loyalka,

Dissertation Co-Supervisors

MAY 2015

The undersigned, appointed by the dean of the Graduate School,

have examined the Dissertation entitled

GENERATION OF GRAPHITE PARTICLES BY ABRASION AND THEIR CHARACTERIZATION

Presented by Raymond Steven Troy

A candidate for the degree of Doctor of Philosophy

And hereby certify that, in their opinion, it is worthy of acceptance.

Professor Robert Tompson

Professor Tushar Ghosh

Professor Sudarshan Loyalka

Professor Mark Prelas

Professor Dabir Viswanath

ACKNOWLEDGEMENTS

I would like to thank my advisors Profs. Robert V. Tompson, Tushar Ghosh, and Sudarshan Loyalka and Profs. Mark Prelas and Dabir Viswanath of the Nuclear Science and Engineering Institute for providing me with guidance, help and resources. Additional thanks, for all the knowledge they have imparted to me as well as the freedom they have allowed me to have while completing this work.

This research has been supported by a Nuclear Energy Initiative (NERI-C; grant DE-FG07-07ID14892, 08-043) grant of the U.S. Department of Energy. Partial support was provided by a Department of Education GAANN Grant. I would like to also thank Dr. Lynn Tipton, Dr. Rajesh Guttti, Dr. Zebediah Smith, Brian Samuels, Dr. Tom Boyle, Lou Ross, Paul Leslie, Leroy Lee, Matt Simones, Nidia Gallegos, and Tyler Rash for their help with various aspects of the work.

TABLE OF CONTENTS

LIST OF TABLES

LIST OF FIGURES

Figure Page

CHAPTER 1. INTRODUCTION

The goal of this work is to gain insights into abrasion related issues that have applications for the Pebble Bed Reactor (PBR). The PBR is a generation four reactor that is a candidate to replace current light water reactors in the future. There are many unique and advantageous things about the PBR such as the fuel, inherent safety in the design, higher fuel burn up, and increased efficiency due to higher operating temperatures. For all these advantages, there are a few things that need to be explored and some questions answered before this type of reactor is licensed and put into operation.

The defining feature of the PBR is the fuel as well as the overall design of the reactor. A pebble bed is mainly comprised of a pressure vessel and fuel, where graphite is the moderator and helium is the coolant. The design of the fuel is inherently safe as it is constructed of tri-isotropic (TRISO) fuel that is encased in graphite spheres (pebbles). The encasing graphite has very good structural properties as well as a very high melting temperature make a "melt down" very unlikely. This protective graphite layer acts as the moderator for the reactor. This fuel design is a look into the future but because of the design, there are some operational challenges. As the reactor is operated, pebbles are introduced at the top of the reactor and taken out of the reactor in a continuous cycle, referred to as online refueling. Due to this constant pebble motion abrasion occurs between the pebble and other pebbles and the pebble and other reactor components, such as the pressure vessel. Due to this abrasion particles are produced, herein referred to as dust.

During the rigorous licensing and safety analysis of the reactor, many things are investigated, modeled, and explored. One staple of the safety analysis is a loss of cooling

accident (LOCA) caused by either a pressure vessel breach or a double-ended guillotine break of the largest cooling piping. In the current commercial light water reactors, when a LOCA occurs water gushes out into the reactor building releasing radioactivity. When the same accident happens in a PBR, helium is released as well as the dust that is produced by the operation of the reactor. In order to license the reactor, the amount of radioactivity that the dust carries must be known to calculate dose to the public, evacuation zones, and worker evacuation.

The aim of this research is to collect data about dust produced in a PBR so it can be used for many purposes, such as licensing.

This Dust production phenomenon has been known for many years and was the focus of one master's dissertation entitled, Graphite Particle Characterization. In that publication, information about the dust was collected and produced in a point contact spinning manner using commercially available graphite.

In this present research, further work has been done in further characterizing the dust, the methods of dust production, as well as the effect of different graphites on dust characterization. In this work two studies were performed and both were performed in a dry air atmosphere. Both studies characterized the dust by measuring, loading, spinning or sliding speed, size distribution, shape, surface area, pore volume, surface roughness, humidity, temperature and wear rate. To further the usefulness of the data, equations were fitted to the size distributions and reported in tables following a log normal distribution. The first used sliding abrasion as the dust production mechanism where the variables changed were loading and sliding speed. The second study used spinning as the

dust production mechanism and the variables changed where the type of graphite (commercial and nuclear grade) as well as loading and spinning speed.

In regards to the first study, I have used a commercial-grade graphite in our experiments and have generated size distributions for the abraded particles. I have also fit lognormal functions to those size distributions (for use in computer codes), determined particle shapes, measured temperature and humidity during the tests, measured and calculated wear rates, measured the surface roughness of both pre-test and post-test samples, particle surface areas, pore volumes, and pore volume distributions of particles produced during abrasion of graphite surfaces under different loadings and sliding speeds. The experiments showed that as loading (analogous to pebble depth in the reactor) and sliding speed increase so do the wear rates and numbers of particles produced, while surface roughness decreases, increases, and then decreases. Brunauer-Emmett-Teller measurements show that abrasion increases surface area from 0.583 $m^2 g^{-1}$ in the bulk material to 555 $m^2 g^{-1}$ in material abraded at high loading and high sliding speed. In all, my research shows that pebble abrasion is a complex process that is not constant during operation and thus should be considered for future work.

In regards to the second study, I have used a commercial non-nuclear grade graphite in my experiments as well as a nuclear grade, MLRF1. The samples started with point contact of two spheres with one being held stationary and the other rotated while under loading. To better understand this type of particle generation, I have modified and used our existing test apparatus to achieve rotational abrasion in a 1% - 5% relative humidity air environment. I have used both a commercial non-nuclear grade graphite and a nuclear grade, MLRF1, from SGL Carbon. In both cases, I used two spheres with one

being held stationary and with the other being rotated while under load and in contact with the first. I have obtained size distributions for the abraded particles. I have also fit lognormal functions to those size distributions (for use in nuclear computer codes), determined particle shapes, measured chamber temperature and humidity during the tests, measured and calculated wear rates of the spheres, measured the surface roughness of both pre-test and post-test samples, and measured particle surface areas, pore volumes, and pore volume distributions of the particles produced during the abrasion of the graphite surfaces under different loadings and with different rotating speeds. I also carried out additional tests to measure the surface temperature near the contact point. The experiments showed that as loading (analogous to pebble depth in the reactor) and rotation speeds increase, so do wear rates, concentration of particles and particle surface area. The shape of the dust particles was in every case non-spherical, as one would expect. The surface area of bulk commercial graphite is above 0.58 $m^2 g^{-1}$ and bulk MLRF is above 2.78 $m^2 g^{-1}$. After testing, abraded particle surface areas were observed to increase to 493 $m^2 g^{-1}$ for commercial and 545 $m^2 g^{-1}$ MLRF1. Wear rates of the spheres during testing were observed to range from 0.003 to 0.07 g min^{-1} per contact site. The upper limit on the size of the abraded particles that was observed was less than about 4000 nm.

CHAPTER 2. SLIDING ABRASION

INTRODUCTION

Graphite dust production in one of the current fourth generation reactor candidates; the pebble bed reactor (PBR), has received significant attention. This dust is produced in many ways during the operation of the reactor such as in the fuel handling system, by pebble on pebble abrasion, and by pebble on reactor component abrasion. Characterization of the produced dust is needed for the future of this reactor configuration for maintenance, licensing, safety analysis, and operation.[1] The PBR uses tri-isotropic (TRISO) fuel that is encased in graphite spheres (pebbles) and the graphite acts as the moderator, as a protective layer, and as structural material. As the reactor is operated, dust is produced and even though TRISO fuel is very robust, this graphite dust interacts (absorption, adsorption, reaction) with fission products (gases, vapors, and solids) and can act to either facilitate or hinder their transport.[2]

A general survey of graphite dust has been given by Cogliati, et al.[2] There have been many other works in analyzing graphite wear, particle generation and graphite dust.[3-7] There have been some other publications on temperature effects,[8] atmosphere effects,[9-16] and friction effects[17-20] which have studied different aspects of particle generation but not much has been done in terms of characterizing the dust. Luo et al.[21] studied the effects of temperature on the coefficient of friction on IG-11 reactor grade graphite. Their experiments were designed to test graphite-graphite and graphite-stainless steel wear at different temperatures. The abrasion was through sliding on a high-frequency, linear-oscillation (SRV) standard wear performance tester, which has a repetitive sliding/lapping action. Luo et al. analyzed the wear extent (of each sample),

temperature, wear rates (of each sample), SEM images, and surface area projections were calculated from those SEM images. Their experiment was conducted in a helium environment and they calculated wear by mass differences during the test. Their loading was 30 N and their stroke length was 2 mm at a 10 Hz frequency with temperatures of room temperature, 100, 200, 300 and 400 °C. As temperature increased so did the extent of the wear and the wear rate. The wear extent at room temperature for the upper sample in the graphite-graphite interaction was roughly 1.0, 1.3, 1.8, 2.0, and 2.3 μg for 180, 240, 420, 580, and 750 m sliding distances, respectively. The wear extent at room temperature for the lower sample and graphite-graphite interaction was roughly 1.9, 2.0, 2.05, 2.1, and 2.3 μg for 150, 290, 420, 580, and 740 m sliding distances, respectively. The wear rate at room temperature for the graphite-graphite interaction upper sample was 8.3×10^{-3} μg m^{-1} for the first 30 minutes and then 2.1×10^{-3} μg m^{-1} for the remainder of the test. The wear rate at room temperature for the graphite-graphite interaction upper sample was 11.1×10^{-3} μg m^{-1} for the first 30 minutes and then 1.4×10^{-3} μg m^{-1} for the remainder of the test.

Recently Rostamian et al.[4, 22] have reported on experimental data and modelling of wear rates under sliding friction. These authors used a tribometer, and IG-11 in Helium and air environments, in temperatures up to 750 °C and pressures of 1 MPa. They found that the wear rate decreased with temperature (by about a factor of 3 from 200 to 750 °C). The experimental set up did not permit sampling of particles in gas-suspension. The authors carried out SEM analysis of abraded graphite samples and accumulated graphite dust, and found that temperature affects wear formation process. The authors also carried out wear computations using a finite element code ABACUS, and computed

a wear coefficient that depends on asperities and a power law coefficient which were then determined from a fitting process. The computations and experimental results were compared to adjust the wear coefficient, and the coefficient was then used for successful predictive purposes. We should note that these experiments did not provide results on the dust generated and its characteristics.

I have previously reported on particle (dust) generation and characterization from rotational/spinning friction.[23] My focus in this work is on the characterization of particles (dust) generated from sliding friction. With some minor and appropriate modifications, I have essentially used the experimental system and methods of measurement and characterization described in my previous paper. The reported results are new, and shed light on the difference between the effects of rotational/spinning and sliding friction on particle generation and particle characteristics.

EXPERIMENTS

Since I essentially used the experimental system and method described in my previous paper on particle generation by rotational friction,[23] my description here will be brief. The system was designed to study the effect of various parameters such as loading, speed of rotation/sliding, atmosphere, shape of interacting surfaces, and types of graphite. In this work, I changed the loading and rotational/sliding speeds while keeping the overall shape of the interface, the atmosphere, and the type of graphite constant. The graphite hemispheres used in this study were of type GM-101 obtained from Graphtek LLC, and have been described in my previous paper. Figure 1 shows the mounting of hemispheres on the lower plate that is fixed to the apparatus. The experimental chamber is shown in Figure 2. Four fresh unused hemispheres were used in each of the

experimental runs. The three lower hemispheres were stationary and were in contact at three points with the upper hemisphere, which was rotated under load by a milling machine, producing sliding abrasion. The test bed was outfitted with a constant tensioning device so that as the hemispheres wore, the load would remain constant. With the contact points constantly changing size and shape, consistent loading was difficult and the average loading is reported. The acrylic chamber, sample holder and scale, which measured the loading, sat on the deck of the milling machine.

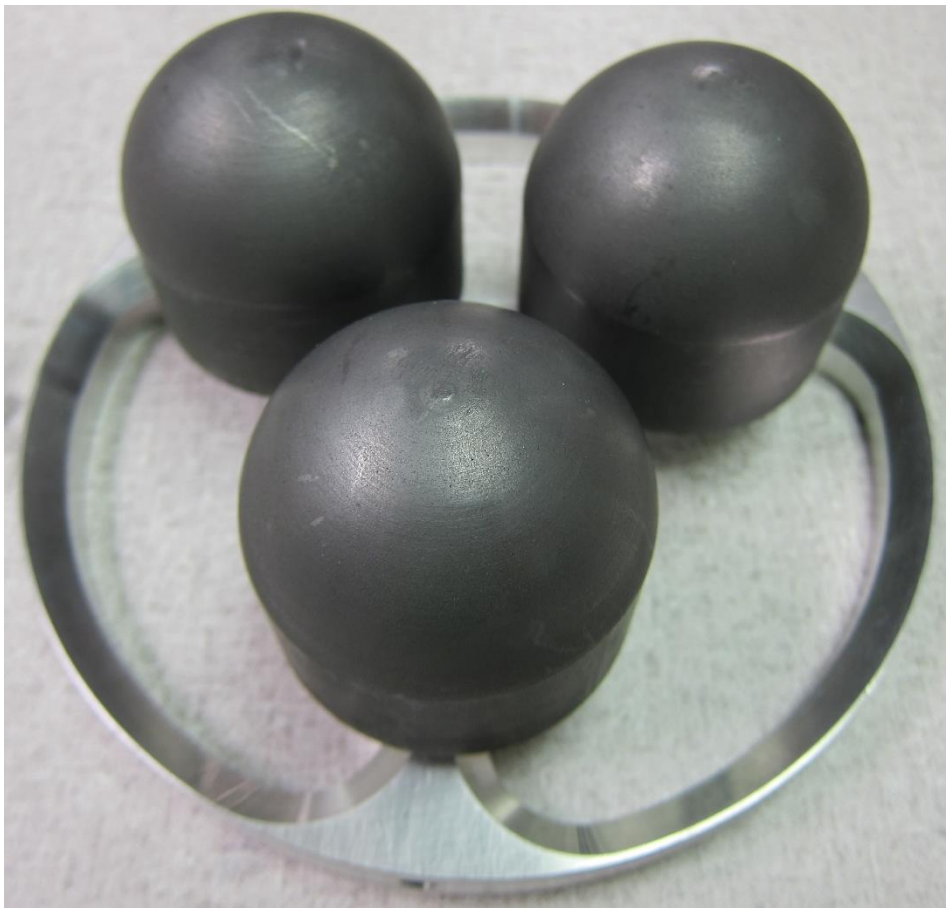

Figure 1. Graphite hemispherical samples mounted on sample holder.

The test bed was constructed using a clear acrylic tube to observe the particle generation during experimentation. A photograph of the experimental system is shown in Figure 3. The rotational speeds of the shaft were preset according to the milling machine manufacturer's specifications. The milling machine was a Central Machinery Geared Head Drill/Mill Machine model 42827. The loading between the two hemispheres is measured by a Mettler Toledo balance, model PBA430, with an IND 56 readout having an accuracy of 0.001 kg with a maximum capacity of 60 kg. The temperature of the tests was room temperature and temperature inside the test chamber was recorded during testing.

Figure 2. Picture of test chamber.

Before each test, the entire apparatus was dismantled and cleaned using soap and water to ensure that no residue or particles from previous tests were still in the chamber. The device was assembled with four new samples. Loading was set, dry air was introduced into the chamber and 10 minutes of background runs were conducted. Once background was collected, sliding was initiated and data collection started. Abrasion

occurred for eight minutes and data was collected for 10 minutes. Data was then post processed.

At the end of the test, dust particles that did not get drawn into the TSI Scanning Mobility Particle Sizer™ (SMPS) and TSI Aerodynamic Particle Sizer™ (APS) but which had settled on the bottom of the cylinder, were collected and viewed under a SEM to determine the shapes of the particles. These settled particles were further analyzed for their shape, surface area, pore volume, and pore size distribution using the BET method.

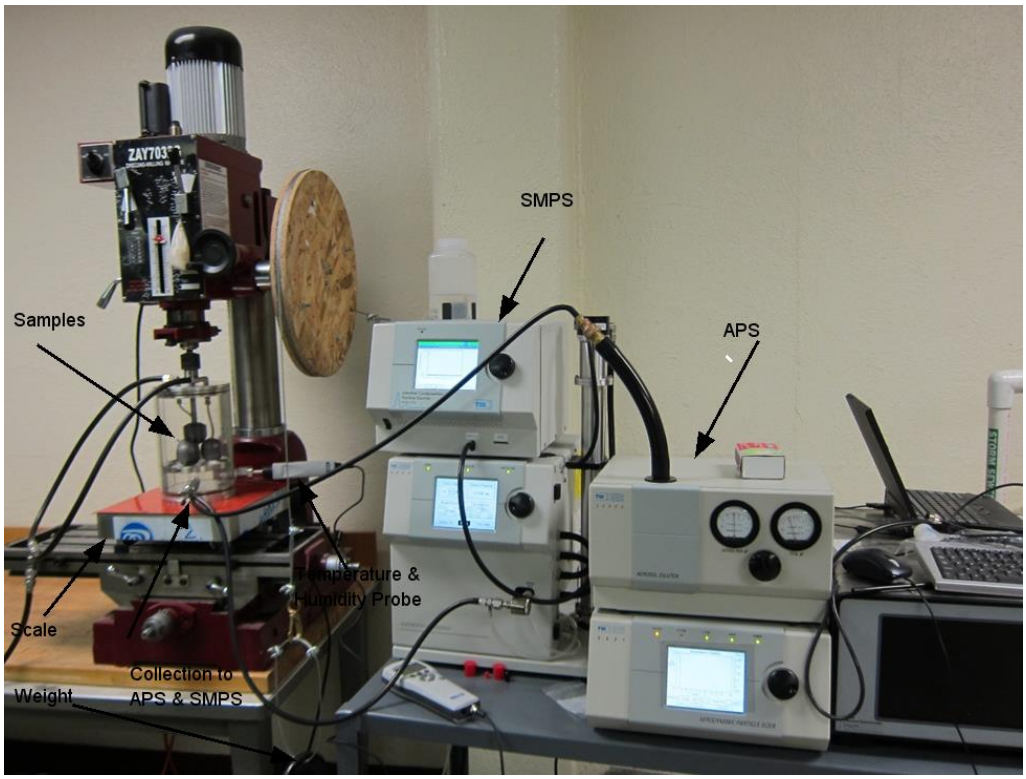

Figure 3. Experimental test bed.

DATA ANALYSIS

As in my previous paper,[23] the particle size distribution was measured by a TSI Scanning Mobility Particle Sizer™ (SMPS™) and a TSI Aerodynamic Particle Sizer™

(APS™), and we refer the reader to that paper for details. The shapes of the graphite particles were determined from scanning electron microscope SEM micrographs from particles that fell to the bottom of the test chamber. A FEI Quanta 600 FEG Extended Vacuum Scanning Electron Microscope (ESEM) was used to take images under a high vacuum ($<6\times10^{-4}$ Pa). The Brunauer, Emmett and Teller (BET) surface area, pore volume, and pore size distribution of the graphite dust particles generated in this work were determined using a Quantachrome® Autosorb-1C instrument equipped with ASiQwin™ 2.0 data processing software. The surface roughness was measured with a Wyko® NT9100 optical non-contact profiling system. The data was gathered and analyzed with the current standard Vision software package.

Humidity was measured with a Viasala humidity probe (DMP74B, calibrated by the factory) coupled to a Vaisala HUMICAP® Hand-Held Humidity and Temperature Meter DM70 with a measurement range of 0 to 100% relative humidity. The dew point range for this probe is from minus 80 to +20 °C with an accuracy of ± 2 °C. The temperature range is from minus 10 to 60 °C with an accuracy of ± 0.2 °C.

To measure the amount of material lost, a balance was used. The balance is an electronic analytical balance model number A-200DS made by Fisher Scientific with a dual range capacity of 200 g/31 g and an accuracy of 0.1 mg/0.01 mg.

EXPERIMENTAL PROCEDURE AND MATRIX

The experiments were conducted in dry air that was piped in at 12 L min^{-1} and which was aimed at the contact area with copper tubing. Excess gas vented to the atmosphere after being filtered. Since both temperature and humidity can potentially

have significant effects on the wear of graphite and, hence, on abrasive particle generation,[24, 25] humidity and temperature inside the test chamber while testing were recorded. No attempt was made in these experiments, to conduct the experiments under specific temperature and humidity conditions other than to make the humidity lower than ambient atmospheric humidity to get to the dusting regime. In the operating reactor, when it is full of helium the humidity is assumed to be close to zero. I wanted humidity to be low to achieve results that were the most applicable to reactor conditions. The loadings and sliding speeds were the only variables considered in the present experimental runs. The ranges of the loadings were chosen based on the loading that is expected in a PBR. A more detailed discussion is given in my previous work.[23]

There were a total of eight tests in this study with two variables (loading and sliding speed) and each test was repeated twice to ensure the abrasion process was repeatable. The loadings and sliding speeds used are given in Table 1. Sliding distance is a function of the rpm, and the radius of contact. Since the contact length did not significantly change and each test was run for eight minutes, this yields a sliding distance of 393 m for tests at 450 rpm and 153 m for tests at 175 rpm.

Test	Loading (kg)	rpm	Sliding Distance (m)
1	17.0	450	393
2	14.7	450	393
3	16.2	175	153
4	16.4	175	153
5	53.9	450	393
6	56.3	450	393
7	51.3	175	153
8	52.5	175	153

Table 1. Experimental Test Matrix. (Dry Air and Graphtek, LLC GM-101 graphite were used in all runs).

RESULTS AND DISCUSSION

Graphite dust particles generated in this work were characterized by various methods to gain a better understanding of the morphology and characteristics of these particles. Two systems, APS and SMPS, were used to determine the particle size distribution over a combined range of 18.1 to 20 000 nm. Some particles settled at the bottom of the chamber, and were analyzed for their shape and size, and surface properties (i.e., surface area, pore volume, pore size and pore size distribution). In addition, wear rate was calculated, lognormal fits were fitted to size distributions, statistical analysis was performed on a size distribution, humidity and temperature inside the test chamber while testing were recorded, and surface roughness before and after testing was recorded. All this data is discussed in the following sections.

SIZE DISTRIBUTION AND LOGNORMAL FIT

The size distributions of graphite dust particles under various loadings as measured by the APS and SMPS systems are discussed below. These distributions were for the particles that remained entrained in air and were carried away to the APS and SMPS systems using their own sampling pump systems. For simplicity, I will use the terms low (14.7 kg-17.0 kg) and high (51.3 kg - 56.3 kg) to describe loading. Similarly, I will use low sliding for 175 rpm and high sliding for 450 rpm. For all eight tests, there was not much difference between the repeated tests under the same loading and sliding speed. Due to the low variance between tests, only four figures will be presented but additional data is available.

Figure 4 is a representative plot from test (lower loading and high sliding), which were corrected for background. Plots for tests one and two were almost identical and is not shown. Particle production in each case stopped at 200 meters of sliding distance and generation did not start again. Particle production started immediately at the beginning of each test, and the concentration (the number of particles per cubic centimeter) level was consistent for the entire test. Very low levels, if any, of particles were larger than 4000 nm. The tail of the distribution is much longer than some of the other distributions in this study.

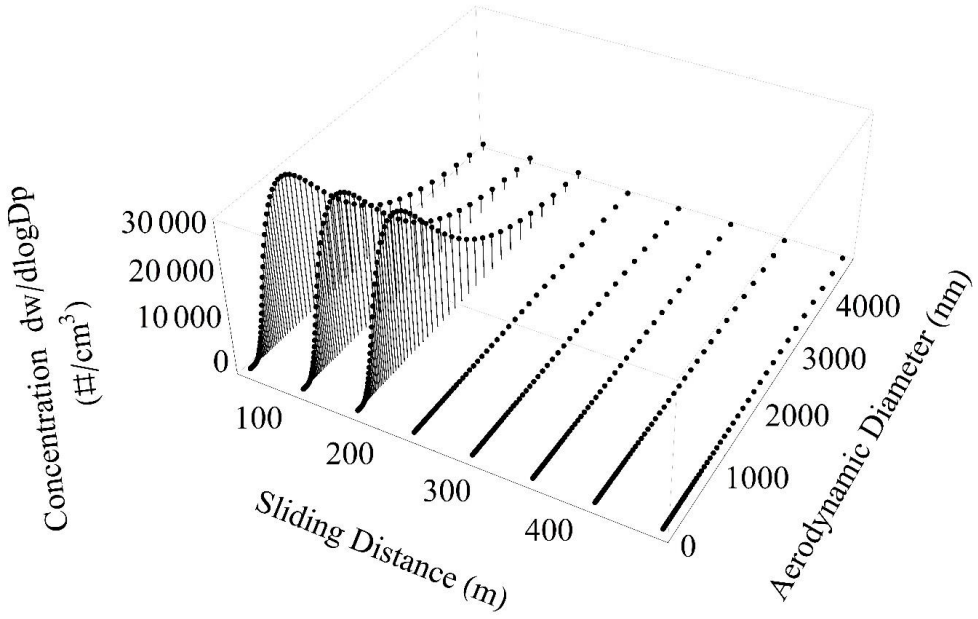

Figure 4. Particle size distribution for 14.7 kg and 450 rpm (test # 2).
This graph has been corrected for background. Similar results were found for test # 1.

Results for test three are shown in Figure 5. Particle size distribution for 16.2 kg and 175 rpm (test # 3).This graph has been corrected for background. Particles were generated for only 19.1 m of sliding distance and particle production stopped after that distance and did not restart for the remainder of the test. In contrast to the low loading and high sliding speed, the concentration of particles is one order of magnitude less. This follows from the lower wear rate due to low loading and high sliding speed. The shape of the distribution is not smooth and has a "waviness" to the distribution. Again, very low levels, if any, of particles were larger than 4000 nm and very similar results were observed for test four.

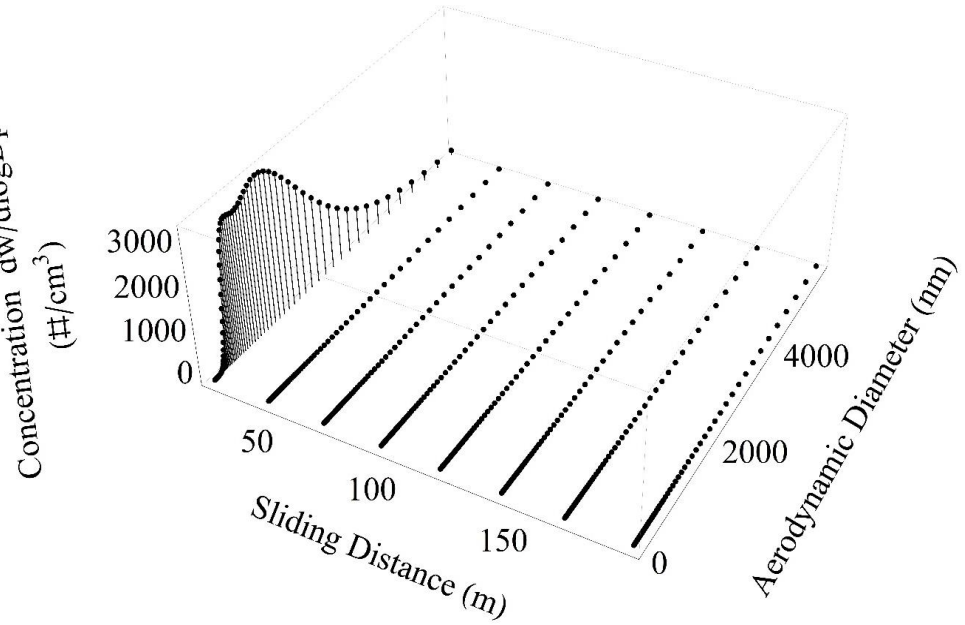

Figure 5. Particle size distribution for 16.2 kg and 175 rpm (test # 3).This graph has been corrected for background. Similar results were found for test # 4.

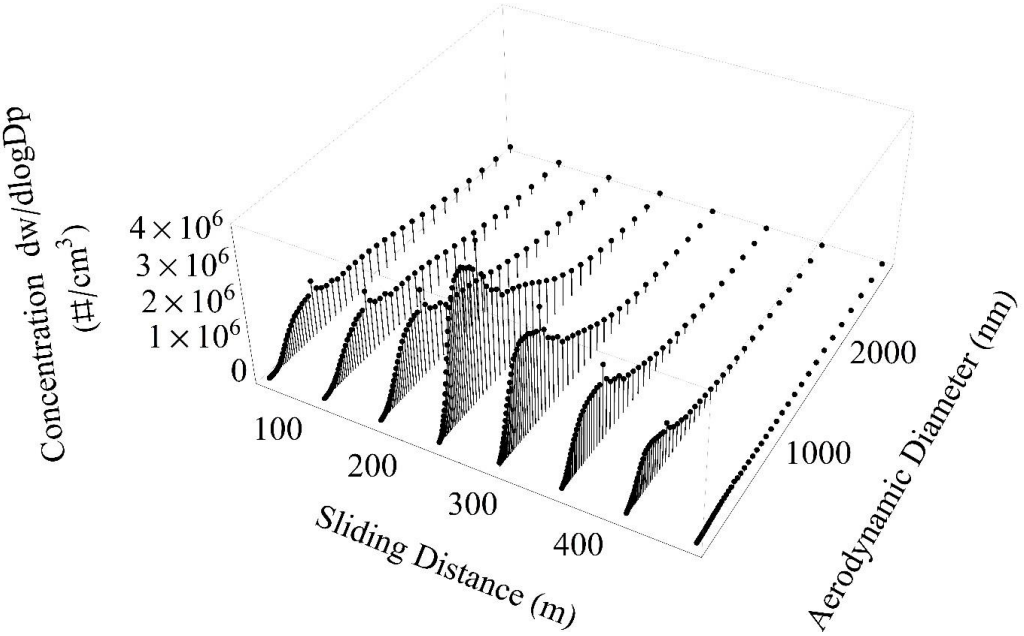

Figure 6. Particle size distribution for 53.9 kg and 450 rpm (test # 5). This graph has been corrected for background. Similar results were found for test # 6.

Tests five and six were conducted at high loading and high sliding speed and a representation of the size distribution from test five can be seen in Figure 6. Again, this

plot was corrected for background. In these tests, the concentrations were much higher than any other test by two orders of magnitude. These tests were meant to simulate a pebble at the bottom of the reactor with all ~300,000 pebbles above it. I note that abrasion stopped only at the limit of eight min (393 m of sliding distance), right in-between sampling points. Particles were generated the whole time that sliding occurred. This graph also shows that only particles that were produced due to abrasion were measured. As soon as the abrasion was stopped the last sampling point (482.2 m of sliding distance) showed no particles measured and this gives us confidence that all the particles measured were directly from abrasion and not particles lingering in the test chamber from all the particles produced. I calculated the sliding distance as,

$$sliding\ distance = \pi\, r\, \omega\, t, \tag{1}$$

where r is the distance from the centerline of the rotating sample to the contact point (0.0347472 m) of the non-rotating sample, ω is the rotational speed, and t is the time. The reported value in all the subsequent tables and figures of 482.2 meters is only a reference to the last data point (10 minutes). This is to signify that all the dust measured was directly from abrasion and not from particles remaining in the chamber. *There was no abrasion after 393 meters of sliding distance.* The sliding distance continued to be measured during the measurement downtimes as abrasion did not stop during these measurement downtimes.

Again, the tails of the distribution were longer at the larger particle sizes. In contrast to the other tests, the range of particle sizes decreased. The range of this graph extended about 2500 nm while the other graphs had been extended to about 4000 nm.

There were no significant particles observed over 2500 nm and this indicates a much narrower distribution. As the test went on, the distribution footprint decreased. In addition, with all the other tests, as the test went on, the particle production was constant or decreasing. In these tests, this was not the case, as in the middle of the test there was an increase in concentration and decreasing concentrations after that peak concentration. The reason for this observed behaviors are not known. Test six results were very similar to the test five results.

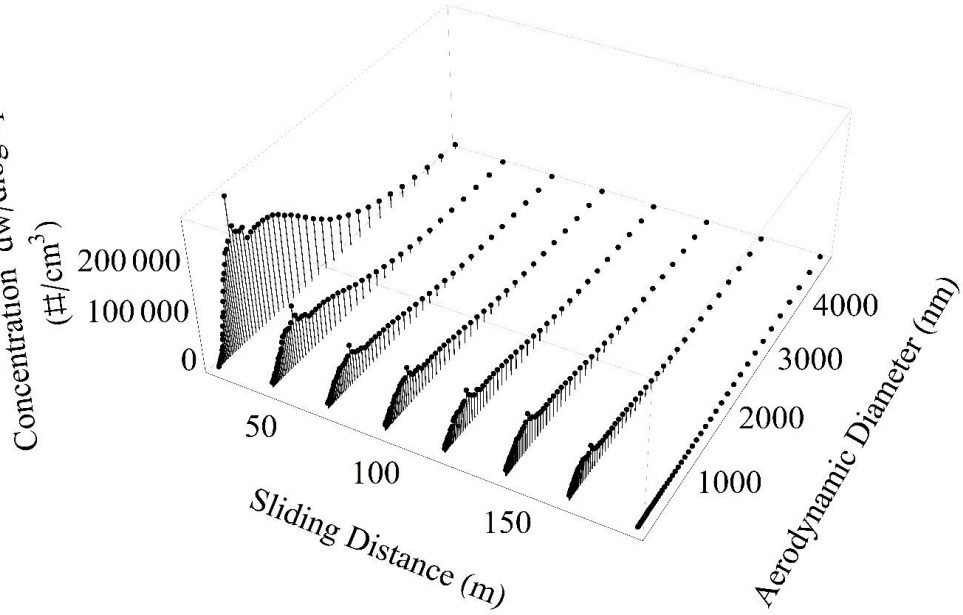

Figure 7. Particle size distribution for 51.3 kg and 175 rpm (test # 7). This graph has been corrected for background. Similar results were found for test # 8.

Tests seven and eight were conducted at high loading and low sliding speed and the representative results from test seven can be seen in Figure 7. Again, this plot has been corrected for background and test eight results were very similar. In this test, particles were produced during the entire test and as soon as the abrasion was stopped, the last sampling point (482.2 m of sliding distance) showed no particles measured. The concentration of particles produced was less than with high loading and high sliding

speed but more than with low loading and either sliding speed. The tails of the distribution were large as is consistent with all the other tests. As the test progressed the distribution became narrower as was also observed in tests five and six. It is interesting to note that there was a large concentration of particles in the first sampling point and that after that it steadily decreased. The shape of this distribution is not smooth and shares characteristics observed in results from tests three and four but which were absent in the results of tests one, two, five and six.

It seems that loading and sliding speed have an effect on the length of time that abrasion occurs. At low loadings (when the pebble is at the top of the reactor) it may produce particles and then stop until the pebble gets lower into the reactor. These experiments also show that the concentration of particles produced due to abrasion can vary widely in size, but that the largest particle size is generally less than 4000 nm and that the most probable particle size observed in all of these tests was about 1 μm.

Although I did not use nuclear grade graphite, our size distributions are in the range that was observed in the AVR reactor. There the dust that was deposited on pipes throughout the AVR reactor was scraped, decontaminated, and de-agglomerated (by ultrasonic treatment and then dried). Optical microscopy showed that the median number particle size was in the range of 0.2 to 0.7 μm whereas the median weight related size was in the range of 0.8 to 1.5 μm. It was also observed that dust adheres very strongly to the pipe walls.[26] The observed particle size in another AVR measurements was 1 μm and less. [27]

From the IAEA TechDoc, "This number-weighted distribution indicates an average dust particle diameter of about 0.6 μm which corresponds to a median diameter

of about 5-10 µm for a particle volume weighted distribution. The size distribution of AYR dust seems to be similar for all filter experiments." [35]

As with all particle sizing experiments, in my experiments also because of deposition in piping and apparatus, not all particles flowed into the particle size measurement instruments. The reported resulting size distribution is thus not the true size distribution, and is likely biased towards smaller size range. I recommend that before my data is used in computer simulations this fact be taken into account.

I conducted each test only twice as the results were similar for each repeated test. A larger number of tests would be certainly desirable for robustness of the data, but I believe the data reported here are quite typical of the results that would be obtained.

STATISTICAL ANALYSIS OF SIZE DISTRIBUTION

I have fitted the measured size distributions with the expression from the TSI software[27]

$$n(d_p) = \frac{A}{(\sqrt{2\pi}\ ln(C))} exp^{-\frac{1}{2}\left(\frac{ln\frac{d_p}{B}}{ln\,C}\right)^2} \qquad (2)$$

where, d_p is the particle aerodynamic diameter in and $n(d_p)$ is the assumed distribution as suggested by the data. A, B, and C are the fit parameters from Eq. 1 and are shown in Table 2. For each test, I have used experimental data at certain sliding distances, and shown the fit parameters in Table 2. I have also shown some indicators of the distribution in

Table 3 as discussed below. For some tests, particles were only produced for a short time and when data is available it is reported in Table 2. Missing values represent sliding distances where a distribution was not produced. Every minute, with a 15 second pause

in between data collection, data was collected and these points in time are what is reported in Table 2. I have reported sliding distance as time and sliding distance are related.

Test Number	Sliding Distance (m)	Goodness	Parameters		
			A	*B*	*C*
1	49.12	0.048	3380	6.63E-07	2.14
2	49.12	0.033	24400	6.08E-07	2.02
	110.53	0.285	289	4.43E-07	2.12
	171.93	0.052	181	6.96E-07	1.94
3	19.10	0.013	9.29E+02	3.33E-07	1.46
4	19.10	0.028	2.20E+03	3.81E-07	1.61
5	49.12	0.052	9.55E+05	5.15E-07	1.98
	110.53	0.043	1.06E+06	4.71E-07	2.05
	171.93	0.042	1.42E+06	4.20E-07	2.04
	233.33	0.042	2.91E+06	3.22E-07	1.97
	294.74	0.049	2.18E+06	2.77E-07	2.07
	356.14	0.058	1.30E+06	2.97E-07	2.04
	417.54	0.061	8.42E+05	2.70E-07	2.06
	482.22	0.121	8.56E+04	3.76E-07	1.97
6	49.12	0.026	3190	5.35E-07	2.32
	110.53	0.035	3730	4.06E-07	2.19
	171.93	0.037	4070	3.71E-07	2.18
	233.33	0.039	3940	3.67E-07	2.17
	294.74	0.037	4330	3.42E-07	2.25
	356.14	0.037	4460	3.83E-07	2.16
	417.54	0.039	2680	3.93E-07	2.11
	482.22	0.048	31.6	3.98E-07	2.25
7	19.10	0.022	181000	5.77E-07	2.03
	42.98	0.071	73300	4.49E-07	2.16
	66.86	0.029	52700	4.15E-07	2.28
	90.74	0.030	52800	4.19E-07	2.3
	114.62	0.026	51800	4.21E-07	2.31
	138.50	0.029	51600	4.03E-07	2.36
	162.38	0.039	41500	3.62E-07	2.37
	187.53	0.182	860	3.54E-07	2.42
8	19.10	0.025	122000	5.79E-07	2.03
	42.98	0.036	147000	4.76E-07	2.09
	66.86	0.043	111000	4.75E-07	2.1
	90.74	0.034	103000	4.92E-07	2.08
	114.62	0.030	110000	4.81E-07	2.09
	138.50	0.037	93400	4.83E-07	2.11
	162.38	0.033	97800	4.30E-07	2.15
	187.53	0.268	2960	4.93E-07	1.89

Table 2. Fit Parameters from Eq. 1.

I have reported statistically significant measures for test 5 in Table 3 (as reported directly by the software associated with the instruments). I am not reporting this information for each test as it can be obtained by using the lognormal fits given in Table 2 with Eq. 2. The values in Table 1 were calculated from the TSI software.[34] Descriptive statistics are displayed in Table 3 at each sampling point.

Sliding Distance (m)	Median (nm)	Mean (nm)	Geo Mean (nm)	Mode (nm)	Geo StdDev
49.12	642.27	907.5	691.33	543.71	2.03
110.53	599.29	820.41	598.61	543.71	2.33
171.93	544.5	737.13	542.8	543.71	2.27
233.33	423.87	568.98	432.73	543.71	2.11
294.74	370.94	480.89	352	543.71	2.32
356.14	404.27	504.69	368.76	543.71	2.37
417.54	359.2	466.54	338.51	543.71	2.36
482.22	474.32	645.94	405.17	543.71	2.89

Table 3. Statistical Analysis of Test 5 (53.9 kg and 450 rpm).

SHAPE AND SIZE FROM SEM ANALYSIS

To further characterize the generated particles and abraded surfaces, I used a Scanning Electron Microscope (SEM) to determine the shapes of the particles. As particles were generated, not all of them flowed into the APS and SMPS systems. The particles that settled on the bottom of the chamber were collected and analyzed by SEM. With the lower loading and both high and low sliding speed tests, there were not enough particles produced to analyze. I have shown the most representative images from my tests. In current computer programs, particles are assumed to be spherical and my experiments show that is not a correct assumption as none of the particles are spheres. All of them have jagged edges and are irregular in shape.

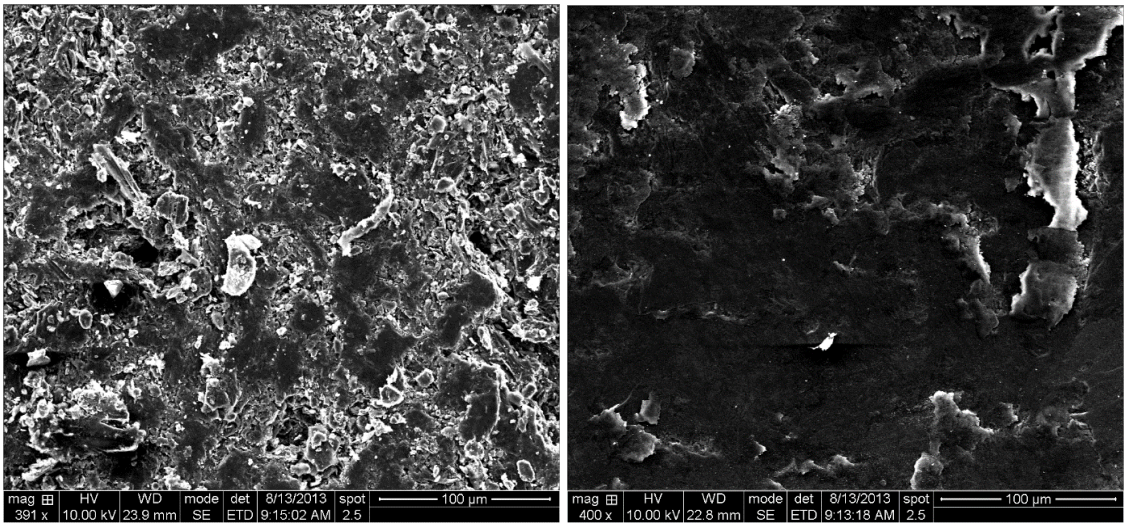

(a) (b)

Figure 8. SEM images of the surface where two hemispherical graphite samples made contact for the abrasion test: (a) before abrasion and (b) after abrasion from test 5.

As one can see from Figure 8., the surface of the graphite greatly changed after abrasion and this is further supported with the surface roughness.

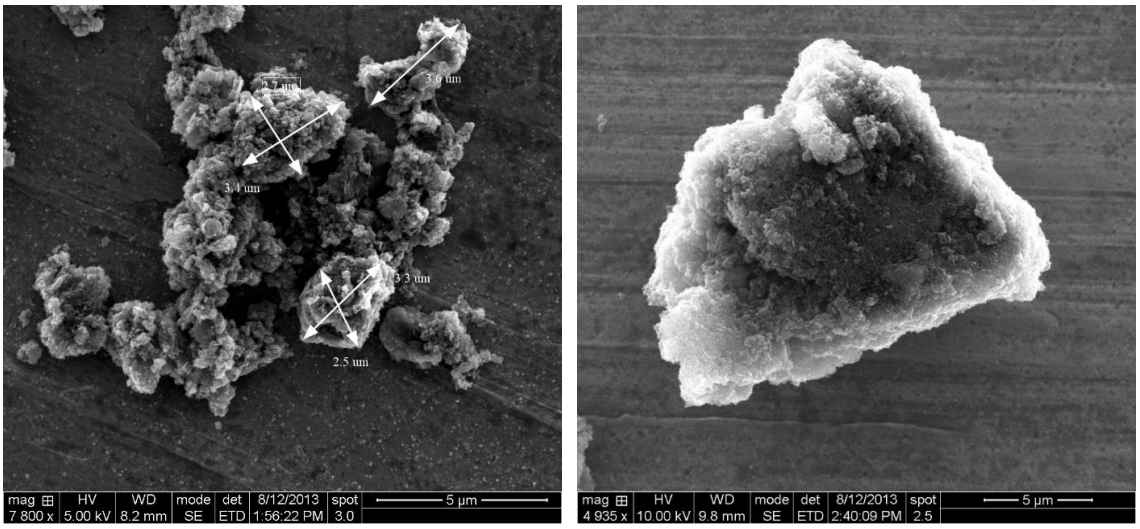

Figure 9. Dust collected from test 5 that fell to bottom of test chamber.

As one can see from Figure 9, the particles are not round or spherical. Note that most particles were less than 2500 nm for this test. This particle is larger than 5000 nm. In Figure 10 you can see the samples before abrasion and after. It is interesting to note the large difference between the two tests in terms of the contact points. In

Table 9 you can see the samples before abrasion and after. It is interesting to note the large difference between the two tests in terms of the contact points.

(a)

(b)

(c)

(d)

(e)

Figure 10. Photos of Samples Before (a) and After Abrasion (b, c, d, e). (b) Test 5. (c) Test 3. (d) Driving Sample Test 5. (e) Driving Sample Test 3.

BET SURFACE AREA, PORE VOLUME, AND POROSITY ANALYSIS

As particles were generated, some fell to the bottom of the test chamber and these were collected for SEM and BET surface area, pore volume, and pore size distribution analysis. The surface properties of the unabraded and three abraded graphites (tests # 2, # 6 and # 8) were characterized by gas adsorption of N_2 at 77 K. The analysis was performed at Oak Ridge National Laboratory using a Quantachrome® Autosorb IC instrument with ASiQwin data processing software. The N_2 isotherms for the four samples are shown in Figure 11. It is observed that, as expected, the unabraded (bulk) graphite shows little nitrogen adsorption, indicative of a very low surface area, while the nitrogen adsorption increases significantly for the graphite dust particles collected during the sliding tests. N_2 adsorption isotherm data were analyzed using the quenched surface DFT (QSDFT) model assuming a slit/cylindrical pore geometry, to obtain the size distribution of open pores, the results are shown in Figure 12.

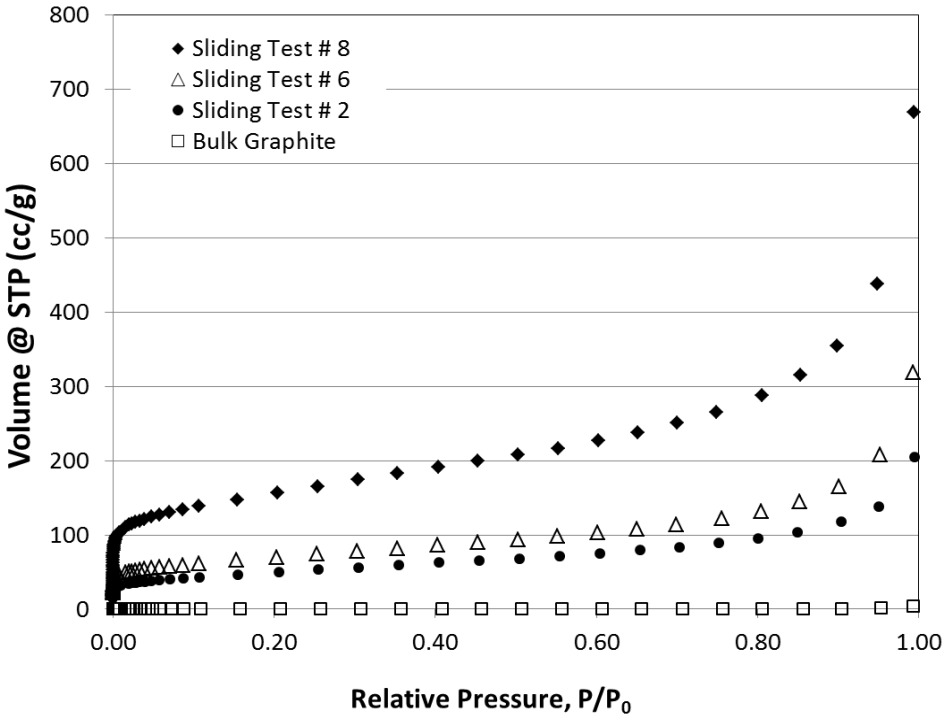

Figure 11. Nitrogen isotherms for bulk graphite and graphite dust samples from three sliding tests (Tests # 2, # 6 and #8).

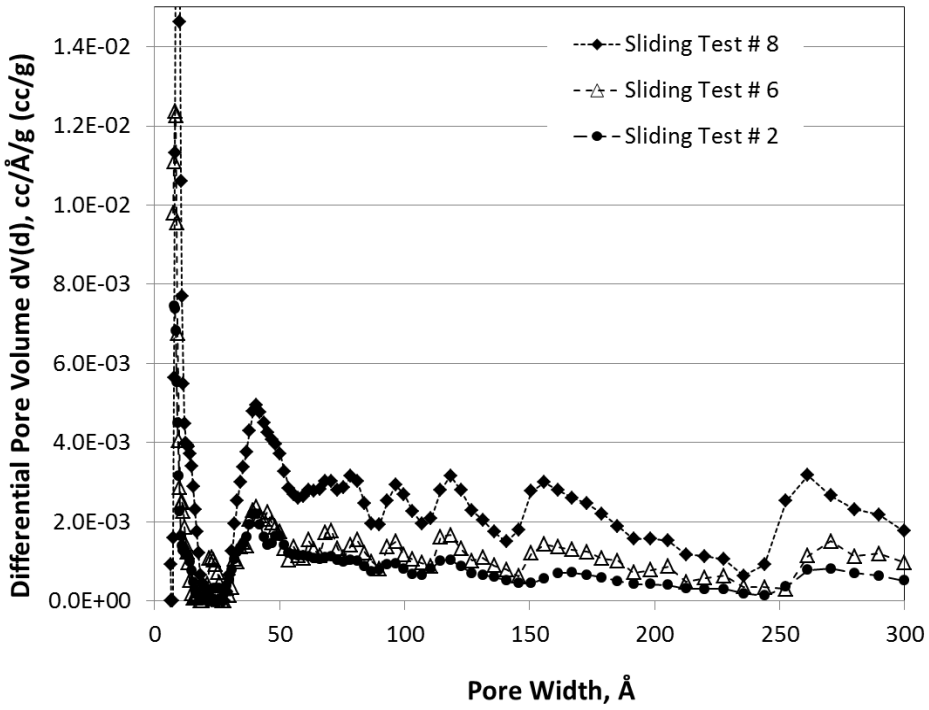

Figure 12. Pore size distribution for graphite dust particles produced during sliding tests 2, 6 and 8.

A summary of the results from the analysis of the N_2 isotherm data are shown in Table 4. It is observed that the surface area of the dust particles generated during the tests increases by approximately 50% when the loading is increased from 14.7 kg to 56.3 kg, and the sliding speed is kept constant at a high value of 450 rpm (sliding test #2 to sliding test # 6). Surprisingly, the surface area of the dust particles more than doubles when the sliding speed is decreased from 450 to 150 rpm and the loading is kept at a high value (56.3 and 52.4 kg). A similar trend is observed for the total pore volume. Although some increase of surface area is expected from the generation of small diameter particles (external surface area), the measured values are significantly higher, indicating that microporosity is being generated within the particles. This porosity within the particles is of great interest, since it could serve as means for adsorption of fission products, and would represent a significant safety issue if released.

Robert et al. [9] investigated the wear debris from a pin on disk experiment for electrographite EG 319 from Carbone Lorraine Society and Morganite MY3 A which was impregnated with copper in argon and nitrogen environments. The surface area of the debris observed was in the range of 140 to 285 $m^2 g^{-1}$. They concluded that the size of wear fragments principally depends on the environment and the normal load.

Further, Hoinkis et al. [28] oxidized graphite pellets which were 10 mm in diameter with a density of 1.7 g cm^{-3}. in CO_2 at temperatures between 1120 and 1170 K and the they observed an increase the BET surface area. They observed a ~10 times increase in surface area. In the work presented here, I saw an increase of 100 times in the surface area.

Zaidi et al. [29] built a tribometer of the pin on disc type located in a vacuum vessel. They used graphitic carbons (supplied by Le Carbone Lorraine) and changed the atmosphere in the vessel. They injected water vapor or hydrogen or oxygen into the vessel and were focused on obtaining surface area and coefficient of friction. They observed wear particle surface areas up to 300 $m^2 g^{-1}$.

In the review work of Londono-Hurtado et al. [30] they gathered literature on the subject of sorption of fission products on carbon. They stated, "the porosity of carbon structures is considered to have a direct influence on sorption and it has been hypothesized that sorption involves both solid-state diffusion and adsorption (sorption onto the surface) of the fission products. " They continue, "there is ample evidence that once porosity is reduced in carbon structures (such as coke, fuel rod matrix, and graphite), there is a decrease on fission product sorption." There is evidence that at low concentrations (i.e., concentrations below 0.02 mg Cs/kg), fission product sorption in graphite is governed by surface area effects rather than by the strength of the binding energies.

	BET Surface Area ($m^2 g^{-1}$)*	Total Pore Volume ($cm^3 g^{-1}$)*
Unabraded (bulk) graphite	0.58	0.006
Abraded graphite Sliding Test # 2	174	0.315
Abraded graphite Sliding Test # 6	246	0.493
Abraded graphite Sliding Test # 8	555	1.035

Table 4. Surface properties of graphite samples.

* Data from nitrogen adsorption at 77 K. The BET surface area is calculated using the Brunauer - Emmett - Taylor equation. The total pore volume is measured at maximum nitrogen pressure.

SURFACE ROUGHNESS MEASUREMENTS

Before abrasion, each type of graphite was measured for surface roughness. After abrasion, each sample was measured for surface roughness and the results are tabulated below. Surface roughness is a highly local measurement and when dealing with material like graphite, that has many pockets, high porosity and surface irregularities measurements many not be consistent. I addressed this by providing averages and to report data at many points. In addition, the sampling size (zoom level) also has an effect on the measurements. When the zoom level is not given it is to be assumed to be 5×.

In my analysis of the surface roughness we used four quantities to characterize surface roughness. R_z is the ten-point height. The average of the ten greatest peak-to-valley separations on the evaluation area and this can be seen in Eq. 8. R_t is the peak-to-valley difference calculated over the entire measured array and this can be seen in Eq. 7. R_q is the root-mean-squared roughness calculated over the entire measured array and this can be seen in Eq. 3. R_a is the average roughness calculated over the entire measured array and this can be seen in Eq. 7.

$$R_a = \frac{1}{n}\sum_{i=1}^{n}|y_i| \quad (3)$$

$$R_q = \sqrt{\frac{1}{n}\sum_{i=1}^{n} y_i^2} \quad (4)$$

$$R_v = min\ y_i \quad (5)$$

$$R_p = max\ y_i \quad (6)$$

$$R_t = R_p - R_v \quad (7)$$

$$R_z = \frac{1}{10}\sum_{i=1}^{10} max\ R_{t,i} \quad (8)$$

These equations can be seen in Bushan's work.[31] A table of these values can be seen below in Tables V-VIII.

Sample Number	R_a	R_q	R_z	R_t
1	8.91	11.92	83.40	92.65
2	2.42	3.20	28.44	37.20
3	1.94	2.60	25.58	34.22
Average	**4.42**	**5.91**	**45.81**	**54.69**

Table 5. Surface Roughness of Pre-Abraded Sample.

Test Number	Sample Number	R_a	R_q	R_z	R_t	Driver
8	25	10.06	12.38	166.11	184.86	Yes
8	26	4.41	5.75	124.03	173.81	No
8	27	11.41	13.23	150.18	189.85	No
8	28	11.03	13.05	113.6	170.76	No

Table 6. Surface Roughness of Abraded Samples from Test 8 (52.5 kg 175 rpm).

Test Number	Sample Number	R_a	R_q	R_z	R_t	Driver
5	29	2.31	3.07	108.41	165.13	Yes
5	30	6.42	8.13	128.12	185.26	No
5	31	2.38	3.24	114.29	171.41	No
5	32	2.74	3.71	82.54	163.11	No

Table 7. Surface Roughness of Abraded Samples from Test 5 (53.9 kg 450 rpm).

Test Number	Sample Number	Magnification	R_a	R_q	R_z	R_t	Driver
3	9	20×	0.49	0.64	9.51	12.54	Y
3	9	50×	6.31	0.4	3.75	4.31	Y
3	10	20×	0.26	0.33	3.73	5.3	N
3	10	50×	1.64	2.04	24.33	35.42	N
3	11	20×	1.12	1.38	10.61	17.17	N
3	11	50×	0.4	0.49	3.1	3.7	N
3	12	20×	0.44	0.54	3.19	3.55	N
3	12	50×	0.74	0.86	5.46	5.84	N
4	13	20×	0.44	0.57	10.27	39.16	Y
4	13	50×	3.14	4.48	41.09	58.73	Y
4	14	20×	0.34	0.43	3.68	7.38	N
4	14	50×	0.79	0.92	5.27	5.83	N
4	15	20×	0.84	2.19	12.16	14.91	N
4	15	50×	0.63	0.75	4.34	14.66	N
4	16	20×	1.49	1.94	40.51	64.27	N
4	16	50×	0.3	0.38	7.37	23.4	N

Table 8. Surface Roughness of Abraded Samples from Test 3 and 4.

The samples in Tables 6 - 8 were collected using the widest sample area available on the instrument for the abraded surface. The Wyko® NT9100 has four different zoom settings 2.5 ×, 5×, 20× and 50× to change the area measured. I have found that surface roughness is very location specific and can vary location to location as well as in the size of the measurement area. In general, but not a rule, the smaller the sampling area (20×, 50×) has lower surface roughness. In Table 8 this was an average of combination of sampling at 20× and 50×. Generally for the samples in Table 8 the 50× had lower values.

Viewing the surface roughness data there is always one sample that is much different from the other samples. Even though all of my surfaces of the test bed were machined to ensure proper alignment, this uneven wear may be due to unevenness in loading across all samples. It appears that sliding speed has an effect on surface

roughness. As loading increases surface roughness decreases and this is expected. What is interesting is the comparison of unbraided values to the abraded values. The lower sliding speed seems to leave the surfaces rougher than pre-abrasion and this is not expected. I feel this is due to the manufacturing process of the graphite used.

The surface roughness is a very local property. When obtaining the surface roughness measurements on very small areas (high magnification), an adjacent area can have a very different value. The inclusion of the surface roughness data is meant to show this strong dependence on location and that it is not an inherent consequence of abrasion. The measurements are accurate but the strong dependence on the area selected can give a surface roughness that is not indicative of the entire sample. I am unable to provide an error analysis because of the nature of the Wyko instrumentation that was used.

HUMIDITY AND TEMPERATURE

Throughout testing humidity and temperature were measured inside the test chamber. There was no effort to control either the humidity or temperature but dry air was used to bring the humidity as low as possible to achieve the dusting effect.[8, 24, 25] Dry air was introduced at 12 L min^{-1} into the test chamber which drove humidity to levels below 5% relative humidity. For my purposes, "dry air" is defined as below 5% RH. Previously, it has been defined as 100 ppm or less.

Only one humidity plot will be displayed. Shown in Figure 13 is a representative plot of the humidity from test number five (53.9 kg and 450 rpm). This is a typical plot in that humidity decreases in the latter half of the test. As one can see from

Error! Reference source not found.. that for all the tests humidity ranged from 1.16 % to 4.29 %.

In regards to temperature,

Figure 15 is a representative plot. Temperature always increases throughout each of the tests with the largest increase in test number five (53.9 kg and 450 rpm). This great increase in temperature is expected as this is the highest loading and highest sliding speed tested which would indicate the most friction. It is surprising at just how much heat is generated, in this test there is a ~21 °C difference. There is significant heat produced considering there was convective cooling from the 12 L m^{-1} dry air flow. Also the humidity decreased with increasing temperature. As loading or rpm increased so did the heat produced, which is expected.

In addition to heat, energy is dissipated with sound. While testing, hearing protection was needed due to the amount of sound that was generated.

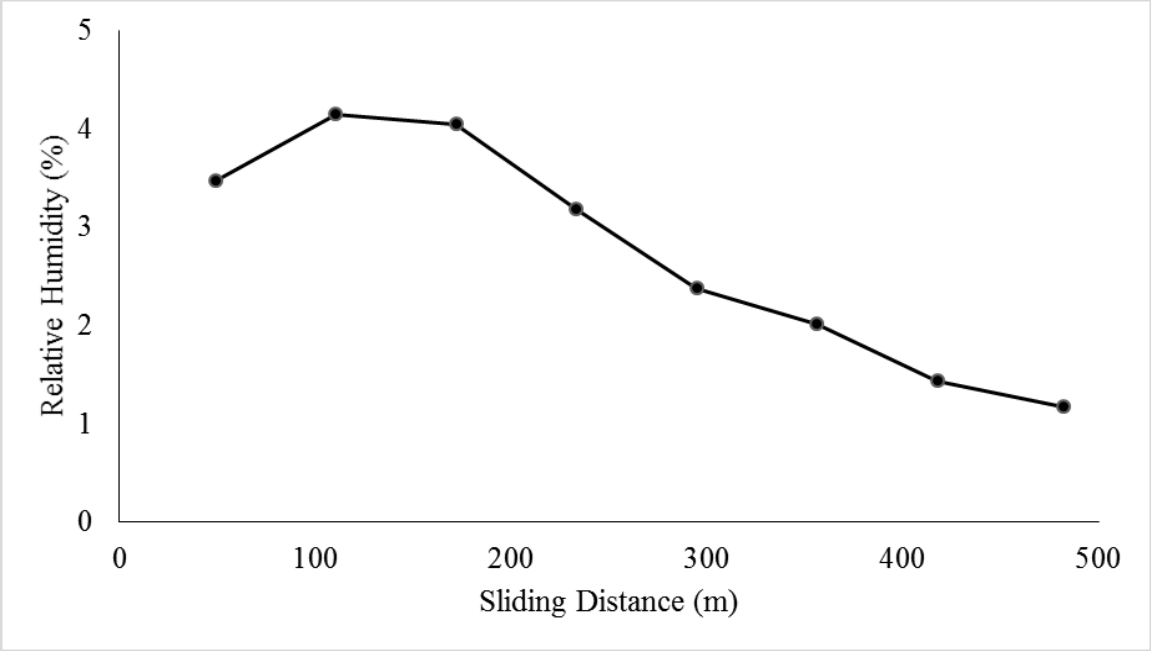

Figure 13. Representative plot of the humidity inside the test chamber during testing. This was from test 5 (53.9 kg and 450 rpm).

In addition to the chamber temperature being measured, after all 8 test runs were completed, I carried out one more test run to obtain the temperature at the surface at one of the points of contact. I attached four thermocouples, attached at four points very close to the point of abrasion, to one stationary sample that was at high loading and high rotational speed and these results are shown in Figure 14.

The surface temperature has an effect on the wear mechanism. Lancaster[24] states that a transition to dusting occurs in the range of 150-200 °C at the contact surface in atmospheric air (50% humidity). Due to my lower humidity environment and the large particle production for high loading (both high and low rotating speeds), I believe that the dusting regime has been achieved. For the lower loading, I am not as confident that dusting has been achieved for two reasons. First, the amount of heat production is low as evidenced by the chamber temperature plots below, indicating a low surface contact temperature. Second, the amount of particle production is low. Due to the particle

production and heat produced I can safely state that I am in the dusting regime for each of the high loading experiments. While I did not reach the 150-200 °C contact temperature that has been observed in the past, dusting was achieved by the low relative humidity and the temperatures of the surfaces of the samples.

Surface contact temperature data is limited tone run of high loading and high rotational speed. In future studies, efforts should be made to measure the surface temperature for full array of tests.

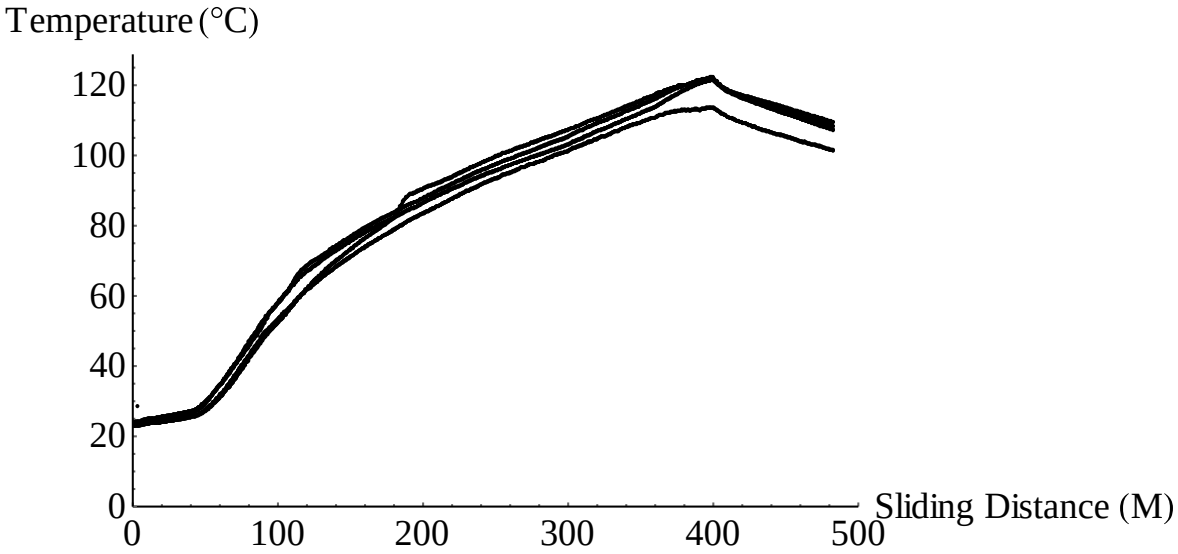

Figure 14. Surface temperature for one stationary specimen for high loading (56 Kg) and high rotational speed (450 RPM).

Lancaster [25] also states the saturation pressure (which is related to contact and environmental temperature), loading and sliding speed (which are related to contact temperature and heat generation) influence in the transition to dusting. In addition, since for each test the results are very similar and the humidity values slightly differed for each test, then dusting was not affected by the small change in humidity. I am not able to

predict if there is a transition to a dusting regime due to humidity in the humidity range of our experiments.

Yen, et al.[8], conducted experiments in nitrogen and air with a low-speed three-pins-on-disc apparatus and a high-energy ring-on-ring apparatus. They made their own carbon-carbon composite material which contained 40% fiber, 47% matrix, and 13% porosity. The humidity for the tests was measured to be between 100 ppm to 50 % RH for both working gases, air and nitrogen. They also observed that dusting is dependent on sliding distance, contact pressure and sliding speed mainly through their influence on contact surface temperature.

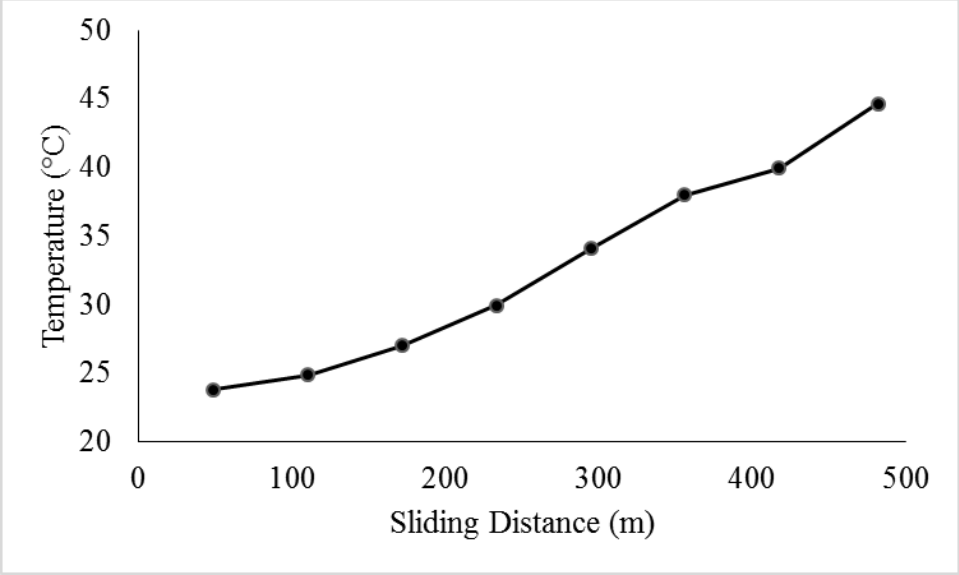

Figure 15. Representative Plot of Temperature inside test chamber during testing. This was from test 5 (53.9 kg and 450 rpm).

Test Number	Max	Min	Average
1	25.55	23.78	23.78
2	25.98	23.48	24.65
3	24.6	23.39	24.00
4	23.23	22.18	22.67
5	44.71	23.73	32.54
6	47.06	22.41	33.25
7	33.68	22.82	27.88
8	30.51	22.64	25.99

Table 9. Temperature values per test presented in degrees Celsius.

WEAR RATE

One desirable quantity to be determined is wear rate. As one can see from Tables 11 and 12, as the loading or rpm increased so did wear rate. Visually from looking at the sample, it came as no surprise that the sample that was driven lost the most mass since it was in contact with three stationary samples. Also each repetition of the test was close in magnitude to the other test and this signifies that graphite abrasion is not as chaotic as one might think.

One must also be cautious of these wear rates as they are not measured at each sampling time but are averaged over the whole test. In some tests, particles were not produced the entire time but the total mass loss was divided by the total time.

I have found that mass loss for 393 meters of sliding distance under high loading was between ~42,300 to ~297,000 µg for my 4 hemisphere configuration. This indicates ~14100 to ~99000 µg per site. Rostamian Hurita et al.[4] had elevated temperatures and mass loss of ~1.7g (170,000 µg) at 200 °C, ~0.1g (100,000 µg) at 400 °C and ~0.4

(40,000 µg) at 750 °C at 400 m of sliding distance. Note that there difference in the experimental conditions of Rostamian et al.[4] and mine. I used loads of~56 Kg (550N) while Rostamian et al.[4] had loads of 10-50 N. Our relative velocities (speeds of rotation) were 0.819 and 0.319 m s^{-1} while Rostamian et al.'s [4] were between 0.01 – 0.05 m s^{-1}

Li and Sheehan[11] carried out sliding friction experiments air at room temperature in air, purified helium and helium containing impurities. For their experiments they used POCO AXF-5Q graphite and a three-dimensional reinforced carbon-carbon composite supplied by McDonnell-Douglass Corporation. Their tests had a sliding distance of 0.339 m and lost 0.00117 g of graphite which is a rate of 3.5×10^{-6} g cm^{-1} (35 µg m^{1}). For comparison with our results of 98 – 7,563 µg m^{-1} for total wear loss one must take into account just one site and divide that number by 3. When divided by 3 my wear rate is 33,000 - 2,972,000 µg m^{-1} per contact site. I have a greater wear rate in our experiments and again I believe the difference due to higher loading and rotational speed. Note that Li and Sheehan used 3.45 MPa of contact pressure with a sliding velocity of 7×10^{-3} mm s^{-1}.

Chen et all., [32] built an apparatus to explore the relationship between pebble feeding velocity in the fuel handling system and wear rate. They used matrix graphite. They concluded that there is a linear relationship between feeding velocity and wear rate. As feeding velocity increases so does wear rate. This is in agreement with my results. The relationship between sliding speed and wear rate is also supported in Chen et al. [33]

From the IAEA TechDoc, a majority of the dust concentration was less than 50 µg m^{-3} and the average was about 5 µg m^{-3} over the final operating years. During normal operation the dust at the AVR was in the range of 1-2 µg m^{-3}.

Test Number	Sample Number	Starting Mass (g)	Ending Mass (g)	Mass Difference (g)	Total material Lost (g)	Wear Rate Per Sample (g min^{-1})	Total Wear Rate (g min^{-1})	Driver
1	37	195.7314	195.6912	0.0402	0.0766	0.0050	0.0096	Yes
	38	191.3831	191.3663	0.0168		0.0021		No
	39	193.3439	193.3377	0.0062		0.0008		No
	40	191.0115	190.9981	0.0134		0.0017		No
2	41	199.2570	199.2100	0.0470	0.0784	0.0059	0.0098	Yes
	42	191.4244	191.4127	0.0117		0.0015		No
	43	198.8207	198.8102	0.0105		0.0013		No
	44	198.4701	198.4609	0.0092		0.0011		No
3	9	192.9773	192.9598	0.0175	0.0256	0.0022	0.0032	Yes
	10	196.3746	196.3719	0.0027		0.0003		No
	11	196.4955	196.4926	0.0029		0.0004		No
	12	195.9835	195.9810	0.0025		0.0003		No
4	13	192.2832	192.2737	0.0095	0.0150	0.0012	0.0019	Yes
	14	195.8220	195.8208	0.0012		0.0002		No
	15	194.1903	194.1880	0.0023		0.0003		No
	16	195.4995	195.4975	0.0020		0.0003		No
5	29	187.9056	187.3153	0.5903	1.7856	0.0738	0.2232	Yes
	30	192.4429	192.3333	0.1096		0.0137		No
	31	187.8823	187.7049	0.1774		0.0222		No
	32	188.6883	187.7800	0.9083		0.1135		No
6	33	198.2524	196.1585	2.0939	2.9723	0.2617	0.3715	Yes
	34	190.7239	190.3760	0.3479		0.0435		No
	35	193.7507	193.4443	0.3064		0.0383		No
	36	195.6972	195.4731	0.2241		0.0280		No
7	21	194.6305	194.1551	0.4754	0.5707	0.0594	0.0713	Yes
	22	199.0076	198.9748	0.0328		0.0041		No
	23	194.1678	194.1325	0.0353		0.0044		No
	24	198.2808	198.2536	0.0272		0.0034		No
8	25	193.0129	192.6728	0.3401	0.4227	0.0425	0.0528	Yes
	26	192.2718	192.2460	0.0258		0.0032		No
	27	197.9584	197.9420	0.0164		0.0021		No
	28	191.7147	191.6743	0.0404		0.0051		No

Table 10. Wear Rate With Respect to Time

Test Number	Sample Number	Starting Mass (g)	Ending Mass (g)	Mass Difference (g)	Total material Lost (g)	Wear Rate Per Sample (μg m^{-1})	Total Wear Rate (μg m^{-1})	Sliding Distance (m)	Driver
1	37	195.7314	195.6912	0.0402	0.0766	102.290	194.911	393	Yes
	38	191.3831	191.3663	0.0168		42.748			No
	39	193.3439	193.3377	0.0062		15.776			No
	40	191.0115	190.9981	0.0134		34.097			No
2	41	199.2570	199.2100	0.0470	0.0784	119.593	199.491	393	Yes
	42	191.4244	191.4127	0.0117		29.771			No
	43	198.8207	198.8102	0.0105		26.718			No
	44	198.4701	198.4609	0.0092		23.410			No
3	9	192.9773	192.9598	0.0175	0.0256	114.379	167.320	153	Yes
	10	196.3746	196.3719	0.0027		17.647			No
	11	196.4955	196.4926	0.0029		18.954			No
	12	195.9835	195.9810	0.0025		16.340			No
4	13	192.2832	192.2737	0.0095	0.0150	62.092	98.039	153	Yes
	14	195.8220	195.8208	0.0012		7.843			No
	15	194.1903	194.1880	0.0023		15.033			No
	16	195.4995	195.4975	0.0020		13.072			No
5	29	187.9056	187.3153	0.5903	1.7856	1502.036	4543.511	393	Yes
	30	192.4429	192.3333	0.1096		278.880			No
	31	187.8823	187.7049	0.1774		451.399			No
	32	188.6883	187.7800	0.9083		2311.196			No
6	33	198.2524	196.1585	2.0939	2.9723	5327.990	7563.104	393	Yes
	34	190.7239	190.3760	0.3479		885.242			No
	35	193.7507	193.4443	0.3064		779.644			No
	36	195.6972	195.4731	0.2241		570.229			No
7	21	194.6305	194.1551	0.4754	0.5707	3107.190	3730.065	153	Yes
	22	199.0076	198.9748	0.0328		214.379			No
	23	194.1678	194.1325	0.0353		230.719			No
	24	198.2808	198.2536	0.0272		177.778			No
8	25	193.0129	192.6728	0.3401	0.4227	2222.876	2762.745	153	Yes
	26	192.2718	192.2460	0.0258		168.627			No
	27	197.9584	197.9420	0.0164		107.190			No
	28	191.7147	191.6743	0.0404		264.052			No

Table 11. Wear Rate With Respect to Sliding Distance.

CONCLUSIONS

These measurements show that the particle size distribution, particle surface areas, particle pore volumes, and particle pore volume distributions, surface roughness, and wear rate all depend on the loading and sliding speed.

As the loading and sliding speed increased so did the concentration as well as the length of time particles were generated. At the highest loading and speed, the distribution was shifted into a smaller size range. This may be due to the increased forces and additional abrasion forcing the particles to a smaller size. I presented representative graphs of particle size distribution as the wear process for two experiments seems to be consistent. More experimental runs would add more statistical confidence to my results. The lognormal and statistical analysis were fitted to those size distributions. The reported size distributions are not the true size distribution, and is likely biased towards smaller size range. I recommend that before our data is used in computer simulations, this fact be taken into account. There was no "break in period" as seen in our earlier work as the particle production started immediately.[23] I feel this is due to the low humidity atmosphere. Also different from previous work is that now the release of a large amount of particles occurred in a short period of time. The particle generation in this work was consistent and not abrupt.

The particles generated are not spherical as can be seen in the SEM images. The particles that were viewed under SEM were ones that had fallen to the bottom of the test chamber and there may be bias. These particle may have been too large or heavy to be carried to the particle sizers. The surfaces of the samples are greatly changed during abrasion as seen from the SEM images. To the naked eye the post abrasion samples look

much smoother and almost glassy and shiny. The samples at higher loading and sliding speed have rings on them where the abrasion was constant for some period of time and then increased causing a new ring. This process was repeated several times but was not reflected in the size distributions. In addition, the size of the wear site greatly depends on loading and sliding speed. These observations are consistent with my previous work.

It was found that significant surface area and porosity are created within the dust particles, and as expected, the surface area increases with loading. However, at higher loadings, the surface area is larger at lower sliding speeds. The mechanism by which the large porosity is created is not completely understood, however, it merits more attention and further investigation since this can strongly affect partitioning of fission products in the gas phase, surfaces and the dust, affecting overall transport of fission products. I have also found that loading and sliding speed affect the surface roughness, and the mechanisms for need to be further understood.

There is a great amount of heat that is produced during these tests especially at the high loading and sliding speeds. This is despite the convective cooling by the dry air. In addition to the heat, a large amount of sound is emitted and hearing protection needed to be worn during testing. This was not observed in my previous work. I was successful in maintaining a low humidity environment for all the tests and further testing should be done in different environments. No attempt was made to regulate humidity to a specific value. Additionally, no attempt was made to regulate temperature to a specific value. Even though these parameters were not regulated, they are important to report. Due to the dust flowing directly into our testing equipment, currently, we cannot perform tests in an elevated temperature testing configuration.

As loading and sliding speed increased so did wear rate. This is to be expected as additional forces abrade the graphite and take material off the sample. Note that the wear rate was calculated using mass loss measured at the beginning and end of the tests unlike some other works.

The present work suggests future tests on different graphite types and grades under a range of controlled environments. I believe that with every graphite the results will differ. The present data are useful in providing a perspective and basis. In my future work, we will report on nuclear grades, but each grade is different on its own. Different shapes of the interacting graphites should be tested to contrast with this and previous works. There is in particular a clear need to elucidate mechanisms that lead to such large intra-particle porosities and surface area, and verify resulting models against data. Also, surface temperature of the contact points will be of interest and should be measured.

REFERENCES

1. C. C. STOKER, L. D. OLIVIER, E. STASSEN, F. REITSMA AND J. J. VAN DER MERWE, "PBMR radionuclide source term analysis validation based on AVR operating experience," *Nuclear Engineering and Design.* 240, 10, 2466-2484, (2010).

2. M. P. KISSANE, F. ZHANG AND M. W. REEKS, "Dust in HTRs: Its nature and improving prediction of its resuspension," *Nuclear Engineering and Design.* 251, 301-305, (2012).

3. M. M. STEMPNIEWICZ, L. WINTERS AND S. A. CASPERSSON, "Analysis of dust and fission products in a pebble bed NGNP," *Nuclear Engineering and Design.* 251, 433-442, (2012).

4. M. ROSTAMIAN, G. JOHNSON, M. HIRUTA, G. P. POTIRNICHE, A. M. OUGOUAG, J. J. COGLIATI AND A. TOKUHIRO, "Computational and experimental prediction of dust production in pebble bed reactors-Part I," *Nuclear Engineering and Design.* (2013).

5. M. ROSTAMIAN, G. P. POTIRNICHE, J. J. COGLIATI, A. OUGOUAG AND A. TOKUHIRO, "Computational prediction of dust production in pebble bed reactors," *Nuclear Engineering and Design.* 243, 33-40, (2012).

6. A. G. POLSON, "Distinct element method analyses of fuel spheres in the PBMR core using RFC3D," 2004, (2004).

7. W. PENG, Y. ZHEN, X. YANG AND S. YU, "Graphite dust deposition in the HTR-10 steam generator," *Particuology.* 11, 5, 533-539, (2013).

8. B. K. YEN, T. ISHIHARA AND I. YAMAMOTO, "Influence of environment and temperature on "dusting" wear transitions of carbon-carbon composites," *Journal of Materials Science.* 32, 3, 681-686, (1997).

9. F. ROBERT, D. PAULMIER, H. ZAÏDI AND E. SCHOULLER, "Combined influence of an inert gas environment and a mechanical action on a graphite surface," *Wear.* 181-183, PART 2, 687-690, (1995).

10. D. H. BUCKLEY AND W. A. BRAINARD, "Friction and wear of metals in contact with pyrolytic graphite," *Carbon.* 13, 6, 501-508, (1975).

11. C. C. LI AND J. E. SHEEHAN, "FRICTION AND WEAR STUDIES OF GRAPHITE AND A CARBON-CARBON COMPOSITE IN AIR AND IN HELIUM," *Wear of Materials: International Conference on Wear of Materials.* 525-533, (1981).

12. K. KIKUCHI, H. KABURAKI, K. SANOKAWA, K. KAWAGUCHI, M. NEMOTO AND S. WATANABE, "IMPURITY GAS EFFECTS ON FRICTION AND WEAR OF HIGH-TEMPERATURE MATERIALS FOR VHTRs," *Nuclear Technology.* 66, 3, 491-502, (1984).

13. J. C. RIETSCH, R. GADIOU, C. VIX-GUTERL AND J. DENTZER, "The influence of the composition of atmosphere on the mechanisms of degradation of graphite in planetary ball millers," *Journal of Alloys and Compounds.* 491, 1-2, L15-L19, (2010).

14. J. J. COGLIATI AND A. M. OUGOUAG, "Pebble bed reactor dust production model," 2009, (2009).

15. J. J. COGLIATI, A. M. OUGOUAG AND J. ORTENSI, "Survey of dust production in pebble bed reactor cores," *Nuclear Engineering and Design.* 241, 6, 2364-2369, (2011).

16. X. SHENG, S. YU, X. LUO AND S. HE, "Wear behavior of graphite studies in an air-conditioned environment," *Nuclear Engineering and Design.* 223, 2, 109-115, (2003).

17. Y.-H. TUNG, R. W. JOHNSON AND H. SATO, "Effects of graphite surface roughness on bypass flow computations for an HTGR," *Nuclear Engineering and Design.* 252, 0, 78-87, (2012).

18. L. XIAOWEI, Y. SUYUAN, S. XUANYU AND H. SHUYAN, "The influence of roughness on tribological properties of nuclear grade graphite," *Journal of Nuclear Materials.* 350, 1, 74-82, (2006).

19. X. LUO, X. LI AND S. YU, "Nuclear graphite friction properties and the influence of friction properties on the pebble bed," *Nuclear Engineering and Design.* 240, 10, 2674-2681, (2010).

20. X. Y. SHENG, S. Y. YU, X. W. LUO, S. Y. HE AND Z. S. ZHANG, "Friction surface analysis on Chinese graphite used in nuclear reactor," *Hedongli Gongcheng/Nuclear Power Engineering.* 22, 5, 401-405+455, (2001).

21. X. LUO, S. YU, X. SHENG AND S. HE, "Temperature effect on IG-11 graphite wear performance," *Nuclear Engineering and Design.* 235, 21, 2261-2274, (2005).

22. M. HIRUTA, G. JOHNSON, M. ROSTAMIAN, G. P. POTIRNICHE, A. M. OUGOUAG, M. BERTINO, L. FRANZEL AND A. TOKUHIRO, "Computational and experimental prediction of dust production in pebble bed reactors, Part II," *Nuclear Engineering and Design.* 263, 509-514, (2013).

23. R. S. TROY, R. V. TOMPSON, T. K. GHOSH AND S. K. LOYALKA, "Generation of graphite particles by rotational/spinning abrasion and their characterization," *Nuclear Technology.* 178, 3, 241-257, (2012).

24. J. K. LANCASTER AND J. R. PRITCHARD, "On the 'dusting' wear regime of graphite sliding against carbon," *Journal of Physics D: Applied Physics.* 13, 8, 1551-1564, (1980).

25. J. K. LANCASTER AND J. R. PRITCHARD, "The influence of environment and pressure on the transition to dusting wear of graphite," *Journal of Physics D: Applied Physics.* 14, 4, 747-762, (1981).

26. J. FACHINGER, A. KUMMER, G. CASPARY, M. SEUBERT, A. KOSTER, M. MAKUMBE AND L. NAICKER, "Examination of dust in AVR pipe components," *2008 Proceedings of the 4th International Topical Meeting on High Temperature Reactor Technology, HTR 2008*, 2009, (2009).

27. H. GOTTAUT AND K. KRÜGER, "Results of experiments at the AVR reactor," *Nuclear Engineering and Design.* 121, 2, 143-153, (1990).

28. E. HOINKIS, H. BEHRET, D. HARTMANN, A. KÖHLING AND E. ROBENS, "The corrosion induced change of pore size distribution and surface area of a fuel element graphite," *Thermochimica Acta.* 29, 2, 345-348, (1979).

29. H. ZAÏDI, D. PAULMIER AND J. LEPAGE, "The influence of the environment on the friction and wear of graphitic carbons. II. Gas coverage of wear debris," *Applied Surface Science.* 44, 3, 221-233, (1990).

30. A. LONDONO-HURTADO, I. SZLUFARSKA, R. BRATTON AND D. MORGAN, "A review of fission product sorption in carbon structures," *Journal of Nuclear Materials.* 426, 1-3, 254-267, (2012).

31. B. BHUSHAN, "Modern Tribology Handbook," *CRC Press*, (2000).

32. Z. P. CHEN, X. W. LUO AND S. Y. YU, "Effect of feeding velocity on wear behavior of graphite ball under elevating process with HTGR fuel handling system," *Yuanzineng Kexue Jishu/Atomic Energy Science and Technology.* 46, SUPPL.2, 853-858, (2012).

33. J. D. CHEN AND C. P. JU, "Effect of sliding speed on the tribological behavior of a PAN-pitch carbon-carbon composite," *Materials Chemistry & Physics.* 39, 3, 174-179, (1995).

34. "Data Merge Software Module Manual, Model 390069," TSI Inc., Shoreview, Minnesota, (2010).

35. K. VERFONDERN et al., "Fuel Performance and Fission Product Behavior in Gas Cooled Reactors," IAEA-Techdoc- 978, International Atomic Energy Agency (1997).

CHAPTER 3. SPINNING ABRASION

INTRODUCTION

Graphite dust production in one of the fourth generation reactor candidates, the pebble bed reactor (PBR), is an area of interest. The Phenomena Identification and Ranking Tables (PIRT) exercise for the Next Generation Nuclear Plant (NGNP) carried out by an expert panel chartered by the US NRC[34] identified the importance of the dust generation phenomenon as 'High' and assessed its state of knowledge as 'Medium' but also felt that adequate models did not exist and there was a major need to develop an adequate modeling capability. This dust is produced in many ways during reactor operations by such things as the fuel handling system, pebble on pebble abrasion, and pebble on reactor component abrasion. This work focuses on the generation and characterization of particles (dust) generated solely by the rotational contact abrasion between two spheres. Characterization of the produced dust for this reactor configuration is needed for future maintenance, licensing, safety analysis, and operational purposes. The PBR uses TRISO fuel in which graphite is the moderator and uses helium as the coolant. A pebble, which contains both the fuel and moderator, has an outer layer that is graphite without fuel and for which there are many graphite variants possible. The coating acts as moderator, protective layer, and structural material within the bed. As the reactor is operated, dust is produced by abrasion and even though TRISO fuel is very robust, this graphite dust interacts (absorption, adsorption, reaction) with any escaping fission products (gases, vapors, and solids) and can potentially act to either facilitate or hinder their transport.[2] Much work has been done in regards to sliding abrasion but little work has been done concerning rotational abrasion. Work in graphite dust production is

needed and Cogliati, et al.[15] has provided a general survey of graphite dust issues in PBRs. I have previous work that summarized the literature on spinning abrasion[23] and another work on sliding abrasion.[35]

EXPERIMENTS

Since I only slightly modified the experimental system and methods described in our previous paper, our description here will be brief. Although this spinning abrasion is not the only type of abrasion possible and does not exactly mimic the forces exerted on the pebbles during routine operation, it provides insights into the generation mechanisms of graphite dust particles, and the effects of various parameters that may influence the particle generation process and the characteristics of the particles produced. The system was designed to study the effect of various parameters such as loading, speed of rotation, atmosphere, shape of interacting surfaces, and types of graphite. In this work, I changed the loading, rotational speeds and the type of graphite, while keeping the shape of the interface (point) and atmosphere (low humidity air), constant. The lower hemispheres/spheres were stationary and were in contact at one point with the upper hemisphere, which was rotated under load by a milling machine, producing spinning abrasion. In this work I have identified the rotating sphere as the 'driver.'

The first type of graphite hemispheres used in this study were constructed of type GM-101 graphite obtained from Graphtek LLC. Various properties of the graphite studied have been provided in my previous work.[23] Figure 16 shows the hemispheres prior to abrasion testing. A threaded insert was pressed into each plug hole so that the graphite hemispheres could be mounted either onto the sample holder or in the chuck of the mill that produced the loaded rotation. The inserts were machined 0.001 in. larger

than the internal diameter of the plug holes to provide an interference fit that prevented the hemispherical samples from misaligning as well as providing enough friction to prevent the machined insert from rotating inside the sample.

Figure 16. Commercial graphite samples mounted on sample holders before abrasion. This grade of commercial graphite was type GM-101 graphite obtained from Graphtek, LLC.

The second type of graphite used in this study was nuclear grade MLRF1 obtained from SGL Carbon, Ltd. Typically, this graphite is extruded into rods which are then machined into spheres measuring 65 mm in diameter. MLRF1 “dummy spheres” from SGL are used for the first core fill in PBRs with a fixed center column and are produced using pitch coke. Various properties of the MLRF1 graphite studied are provided in Table 13. Because the samples were spheres, holding the samples proved difficult and the threaded insert would not work as I wanted to preserve the samples as best I could. Custom sample holders were designed and constructed and they can be seen in

Figure 17. They have a spherical cavity with three set screws around the perimeter to provide the grip needed to transfer loading and rotation.

Manufacturer	SGL Carbon
Grade	MLRF1
Method of manufacture	Extruded
Density	1730 kg m^{-3}
Particle (grain) size	Max of 1 mm
Flexural strength	20 MPa (WG); 16MPa (AG)
Young Modulus	8.7 GPa (WG); 6.5 GPa (AG)
Resistivity	10×10^{-6} Ohm m
CTE	3.3×10^{-6} K^{-1} (WG); 4.4×10^{-6} K^{-1} (AG)
Porosity	14.5%
Thermal conductivity	170 W m^{-1} K^{-1} (WG); 130 W m^{-1} K^{-1} (AG)
Ash content	70 ppm
Boron Content	1 ppm
AG= Against Grain WG = With Grain	

Table 12. Properties of the Nuclear Grade Graphite MLRF1 (65 mm spherical sample).

Figure 17. MLRF1 graphite mounted in sample holders before abrasion.

The test bed was outfitted with a constant tensioning device so that as the hemispheres wore, the load would remain essentially constant. With the contact points constantly changing size and shape, however, consistently constant loadings were difficult to achieve and only the average loadings are reported. The acrylic chamber, the sample holder and the balance, which measured the loading all sat on the deck of the milling machine. A photograph of one sample set up is shown in Figure 18. The test bed was constructed using a clear acrylic tube to observe the particle generation during experimentation. The rotational speeds of the shaft were preset according to the milling machine manufacturer's specifications. The milling machine was a Central Machinery Geared Head Drill/Mill Machine model 42827. The loading between the two hemispheres is measured by a Mettler Toledo balance, model PBA430, with an IND 56 readout having an accuracy of 0.001 kg with a maximum capacity of 60 kg. This balance capacity was selected as it approximates the maximum load that might be expected to exist on a single sphere located at the bottom of a typical PBR core due to the weight of the graphite spheres located above it. The temperature of the tests was room temperature and temperature inside the test chamber was recorded during testing and reported below.

Figure 18. Picture of test chamber with commercial graphite mounted.

Figure 19. Picture of test chamber of MLRF1 graphite mounted.

Before each test, the entire apparatus was dismantled and cleaned using soap and water to ensure that no residue or particles from previous tests were still in the chamber. The device was assembled with two new samples. Loading was set, low humidity air was introduced into the chamber and 10 minutes of background runs were conducted to ensure that the system had been adequately cleaned. Once background was collected, spinning was initiated and data collection immediately started. Abrasion occurred for eight minutes and data was collected for 10 minutes. The collected data was then post-processed.

At the end of the test, dust particles that did not get drawn into the TSI Scanning Mobility Particle Sizer™ (SMPS) and TSI Aerodynamic Particle Sizer™ (APS) but which had settled on the bottom of the cylinder, were collected and viewed under a SEM to determine the shapes of the particles. These settled particles were further analyzed for their surface area, pore volume, and pore size distribution using the BET method.

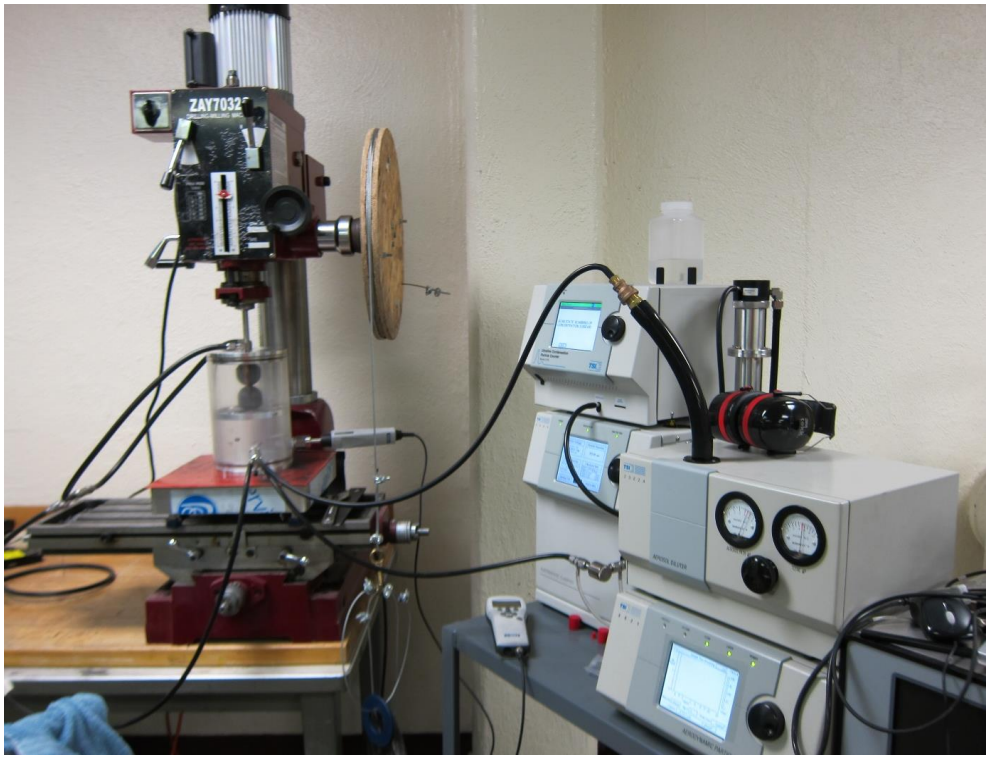

Figure 20. Experimental test bed.

DATA ANALYSIS

As in my previous works, the particle size distribution was measured by a TSI Scanning Mobility Particle Sizer™ (SMPS™) and a TSI Aerodynamic Particle Sizer™ (APS™), and I refer the reader to my previous papers for details.[23, 35] The shapes of the graphite particles were determined from scanning electron microscope SEM micrographs from particles that fell to the bottom of the test chamber. A FEI Quanta 600 FEG Extended Vacuum Scanning Electron Microscope (ESEM) was used to take images under a high vacuum ($<6\times10^{-4}$ Pa). The Brunauer, Emmett and Teller (BET) surface area, pore volume, and pore size distribution of the graphite dust particles generated in this work were determined using a Quantachrome® Autosorb-1C instrument equipped with ASiQwin™ 2.0 data processing software. The surface roughness was measured with a Wyko® NT9100 optical non-contact profiling system. The data was gathered and analyzed with the current standard Vision software package.

Humidity was measured with a Viasala humidity probe (DMP74B, calibrated by the factory) coupled to a Vaisala HUMICAP® Hand-Held Humidity and Temperature Meter DM70 with a measurement range of 0 to 100% relative humidity. The dew point range for this probe is from minus 80 to +20 °C with an accuracy of ± 2 °C. The temperature range is from minus 10 to 60 °C with an accuracy of ± 0.2 °C.

In addition to chamber temperature measurement, after all 16 tests were carried out, four additional tests were conducted measuring the surface temperatures of the graphite near the abrasion points using thermocouples affixed to the stationary sphere with adhesive. The tests were carried out at high loading and high rotational speed and

low loading and low rotational speed for each graphite; totaling four tests. These measurements were not made during the original cohort of tests as they would have interfered with our determinations of the mass losses due to the additional unknown masses of the thermocouple adhesive being present. The temperature was measured by affixing four thermocouples to the surface of the bottom (stationary) sample and data was collected by a Measurement Computing USB-TC-AI data collection system. The error or uncertainty for the T-type thermocouples used, was ±0.035 °C. To measure the total amount of abraded material lost, a balance was used. The balance used was an electronic analytical balance, model number A-200DS, made by Fisher Scientific with a dual range capacity of 200 g/31 g and an accuracy of 0.1 mg/0.01 mg.

EXPERIMENTAL PROCEDURE AND MATRIX

The experiments were conducted in low humidity air that was introduced at 12 L min^{-1} and which was aimed at the contact area between the spheres with copper tubing to facilitate entrainment of the dust produced. Excess gas vented to the atmosphere after being filtered. Since both temperature and humidity can potentially have significant effects on the wear of graphite and, hence, on abrasive particle generation,[24, 25] both humidity and temperature were recorded inside the test chamber while testing. No attempt was made in these experiments, to conduct the experiments under specific temperature and/or humidity conditions other than to make the humidity notably lower than ambient atmospheric humidity to mimic the low humidity environment experienced in the reactor. Of course, in an operating PBR reactor, helium is used as the coolant and the normal humidity is assumed to be virtually zero. I generally wanted the relative humidity to be low enough to achieve results that would be reasonably applicable to

reactor operating conditions even though helium was not being used. The ranges of the loadings were chosen based on the loading that is expected in a PBR. A more detailed discussion is given in my previous work.[23]

There were a total of 16 tests in this study adjusting three variables: loading (high and low), rotational speed (high and low) and two graphites. Each test was then repeated twice to ensure the abrasion process was consistent. The loadings, rotational speeds, and graphites used are summarized in Table 13. With the commercial GM-101 graphite 16 samples were used, two fresh new samples for each test. For the MLRF1 graphite, only eight samples were used but each test was started using fresh, new surface contact points. The high cost of the material was the reason that samples were reused. A test was carried out, measurements were taken and then that same sample was reused but with a fresh contact surface for the second test. The reuse of the samples should have had no effect on the results as fresh contact surfaces were ensured for each test.

Test Number	Loading (kg)	RPM	Graphite*
1	57.54	1500	GM-101
2	51.51	1500	GM-101
3	56.70	1500	MLRF1
4	56.59	1500	MLRF1
5	17.24	1500	GM-101
6	16.58	1500	GM-101
7	17.94	1500	MLRF1
8	16.41	1500	MLRF1
9	50.68	450	GM-101
10	54.50	450	GM-101
11	48.93	450	MLRF1
12	51.27	450	MLRF1
13	15.30	450	GM-101
14	14.48	450	GM-101
15	15.99	450	MLRF1
16	19.00	450	MLRF1

Table 13. Experimental Test Matrix (Conducted in Dry Air).
* GM-101 from Graphtek, LLC and MLRF1 from SGL Carbon, Ltd.

RESULTS AND DISSCUSSION

Graphite dust particles generated in this work were characterized by various methods to gain a better understanding of the morphology and characteristics of these particles. Two systems, APS and SMPS, were used to determine the particle size distribution over a combined range of 18.1 to 20 000 nm. Some particles settled at the bottom of the chamber, and were analyzed for their shape and size, and surface properties (i.e., surface area, pore volume, pore size and pore size distribution). In addition, wear rates were calculated, lognormal fits were fitted to size distributions, humidity and temperature values inside the test chamber while testing were recorded, and sample surface temperatures, and surface roughness values before and after testing was recorded. All this data is discussed in the following sections.

SIZE DISTRIBUTION AND LOGNORMAL FIT

The size distributions of graphite dust particles under various loadings and rotational speeds as measured by the APS and SMPS systems are discussed below. These distributions are for the particles that remained entrained in air and were carried away to the APS and SMPS systems using their own sampling pump systems. For simplicity, I will use the terms low (14.48 kg-19.0 kg) and high (48.93 kg – 57.54 kg) to describe loading. Similarly, I will use low rotation for 450 RPM and high rotation for 1500 RPM. While each test was repeated twice, there were major differences noted in only two of the data pairs and these were the cases with high loading and high rotation for each graphite where maximum experimental variation would be most expected. At all other loadings or rotational speeds, both tests produced results that were very similar. For the lower loading and lower rotational speed very few particles were generated; generally not even enough to create full size distributions.

Figure 21 and Figure 22 show the size distributions obtained for the two tests of commercial graphite at high loading and high rotational speed. While these tests were completed in identical manners, in the second plot there is a great release of particles at one point in time and this behavior is not repeated anytime in the test. In my previous work,[23] this phenomenon was also observed but in another of my work[35], even though each test was repeated twice as in this work, this behavior was not observed at all. Since the previous work where this phenomenon was observed was also concerned with a type of rotational abrasion, this may mean that these sudden releases of particles are inherently associated with rotational abrasive processes. Given the limited number of observed occurrences, however, one might suspect only the normal statistical inhomogeneities in

the morphologies of the processed graphite samples was the cause. Either way, additional work would be needed to confirm any hypothesis or we note these occurrences here only because they might potentially represent significant fractions of any generated particles. This second test was the only time throughout this work that such a relatively high concentration was released. In the first test, particle production increased to a maximum, stayed fairly constant, and then decreased. Most of the particles were below 4000 nm in size and the last data collection (at 10 minutes) shows no particles being collected which gives us confidence that the only particles measured were directly produced from abrasion. In the second test, ignoring the concentration spike that occurred, a behavior similar to the first test can be discerned.

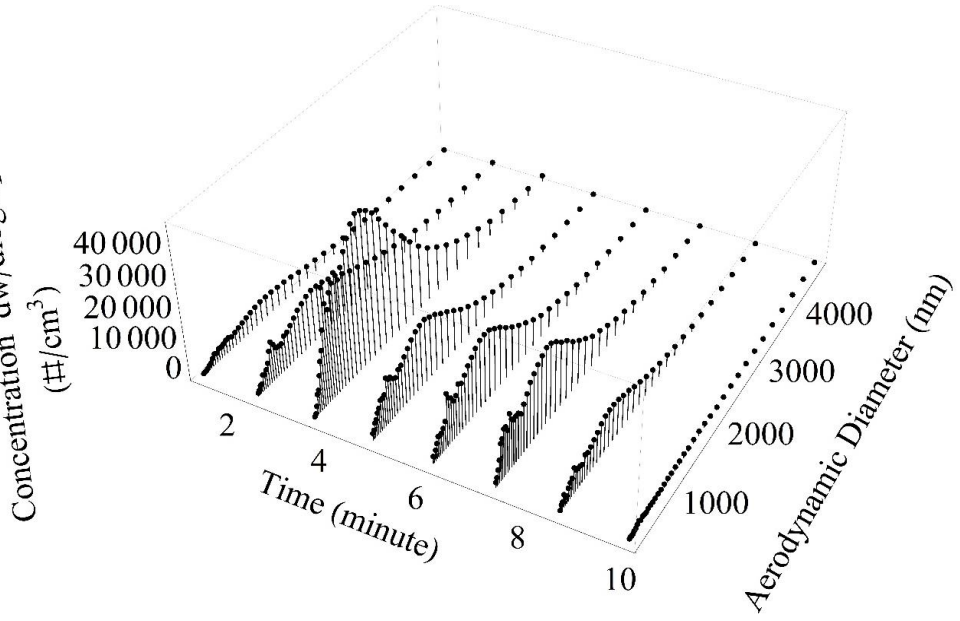

Figure 21. Particle size distribution for 57.54 kg and 1500 rpm for GM-101commercial graphite. This graph has been corrected for background and represents test 1.

Under the same basic conditions, Figure 23 and Figure 24 display the particle size distributions for high loading and high rotational speed for MLRF1 graphite. The first

thing to note is the scale for the concentration of particles. For the same loading as commercial graphite, MLRF1 produced a higher concentration of particles (if the sudden release mentioned previously, is disregarded). Specifically, the concentration is an order of magnitude higher and the size distribution is notably tighter than for the commercial graphite. Also, no very high concentration releases were observed such as the one that was noted previously in the commercial grade graphite under the same conditions. While these two tests produced size distributions that look similar, the difference in the highest concentrations is almost a factor of three. It is unknown why this difference occurred. In both MLRF1 tests the concentrations increase, reach a maximum and then decrease.

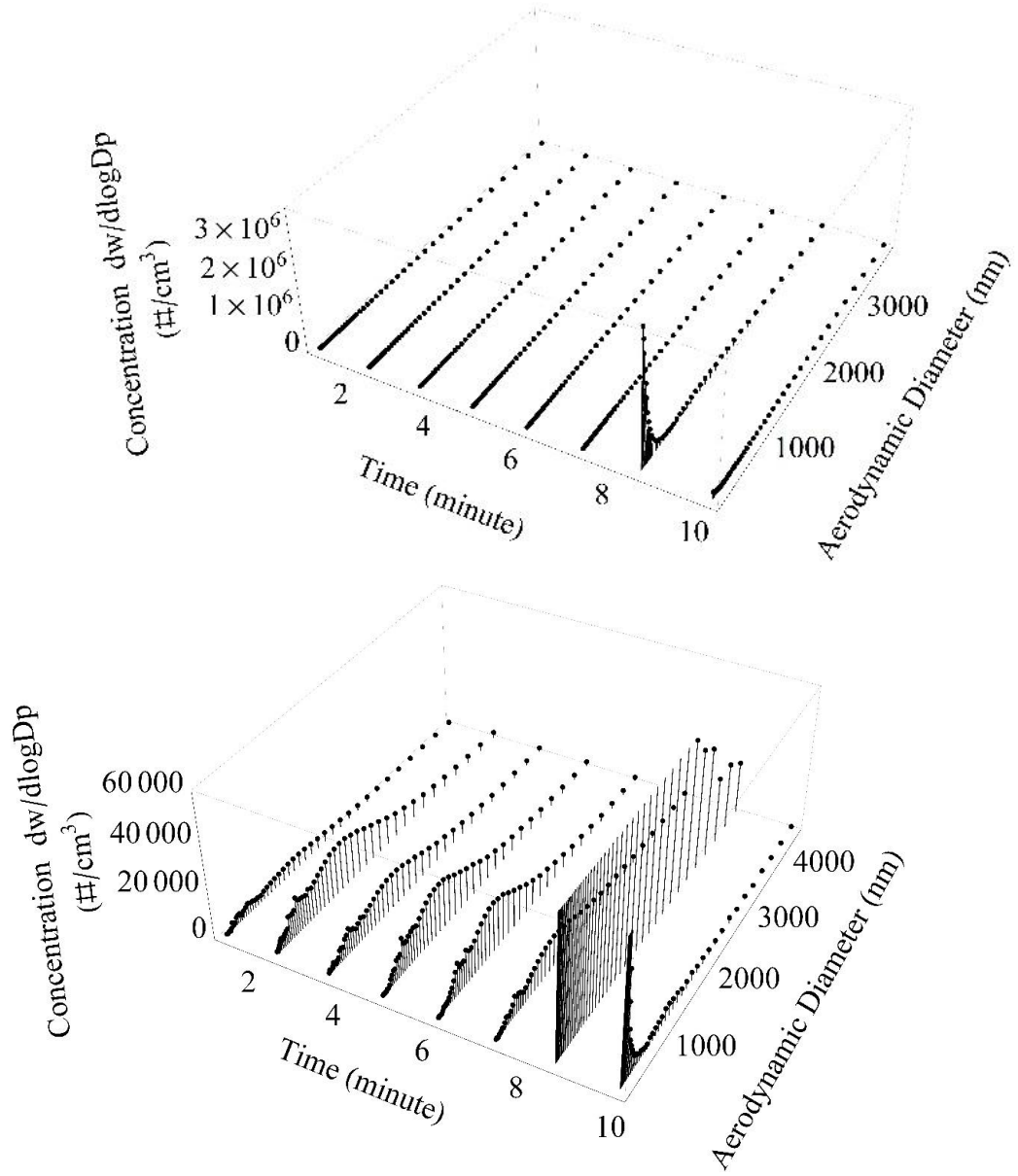

Figure 22. Particle size distribution for 51.51 kg and 1500 rpm for GM-101 commercial graphite. Both graphs have been corrected for background and represent test 2. (a) is presented in a scale similar to other graphs of this type and shows the shape of the distribution as a function of time. (b) is the same graph presented in a scale intended to emphasize the magnitude of the particle burst observed near 8 min.

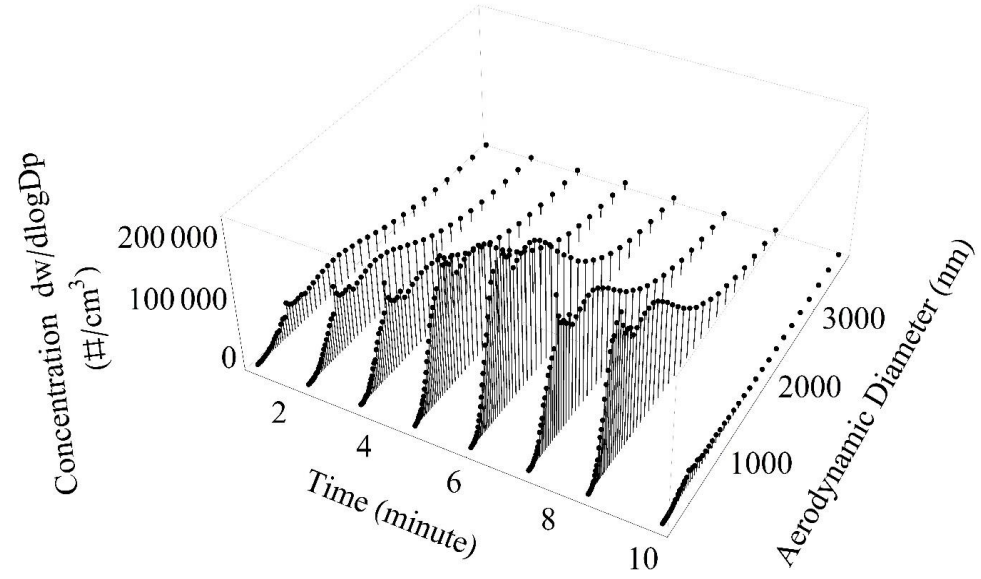

Figure 23. Particle size distribution for 56.70 kg and 1500 rpm MLRF1 graphite. This graph has been corrected for background and represents test 3.

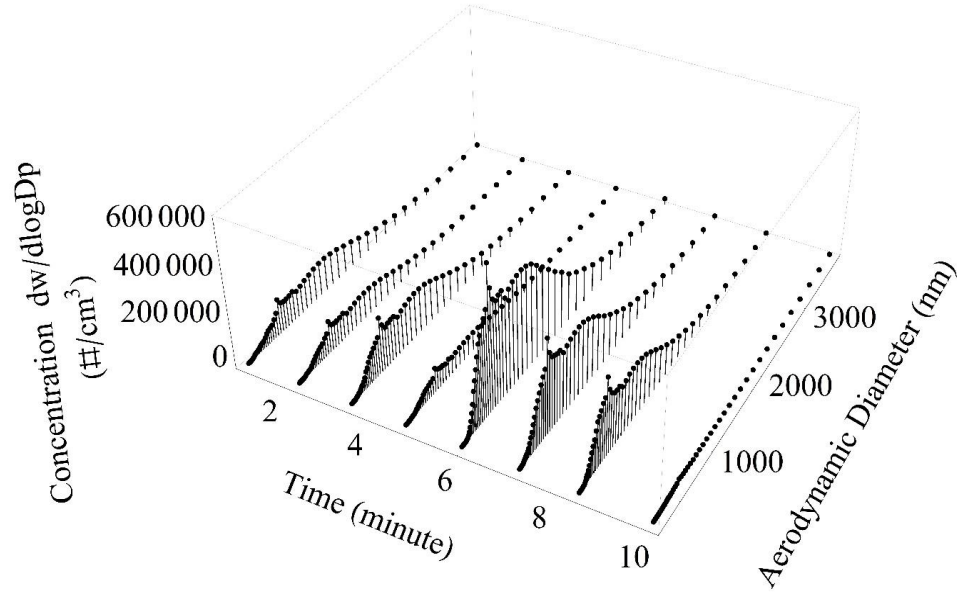

Figure 24. Particle size distribution for 56.59 kg and 1500 rpm MLRF1 graphite. This graph has been corrected for background and represents test 4.

The concentration values for high loading and low rotational speed using commercial graphite are depicted in Figure 25 and Figure 26. There is decrease in concentration from high loading and high rotational speeds and this is consistant with our

past results.[23] As the tests progress, there are not any large concentration peaks such as that observed in the one high loading and high rotational spped commercial graphite test. The maximum concentrations observed in these two test also seem more consistant with each other than was noted in the previous tests. It does seem noteworthy that the distributions found for the MLRF graphite appear narrower than those found for the commercial graphite. In these tests, as before, the abrasion ended at the eight minute mark and at the 10 mintue mark no particles were observed indicating that all particles measured were only from abrasion..

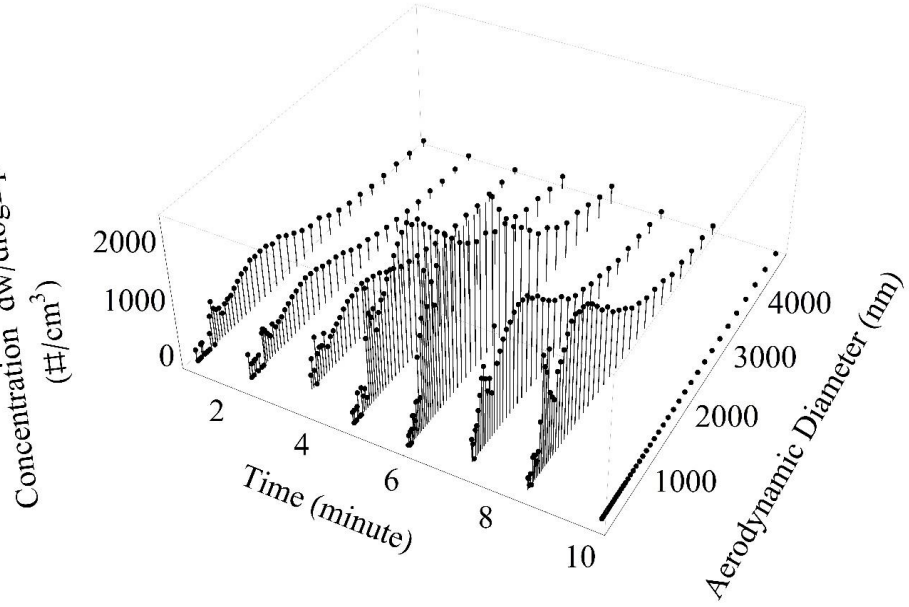

Figure 25. Particle size distribution for 50.68 kg and 450 rpm GM-101 commercial graphite. This graph has been corrected for background and represents test 9.

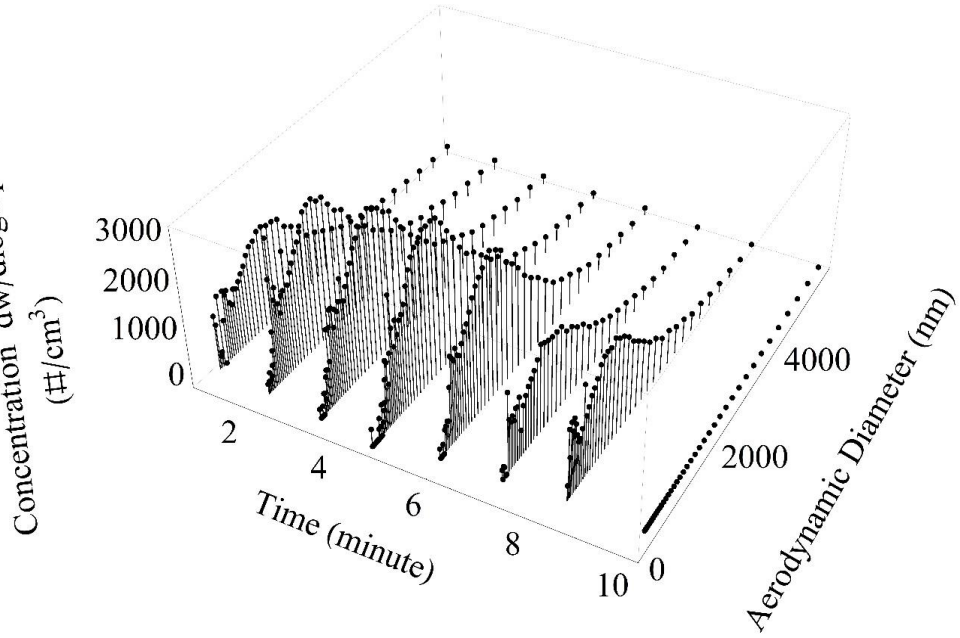

Figure 26. Particle size distribution for 54.50 kg and 450 rpm GM-101 commercial graphite. This graph has been corrected for background and represents test 10.

Figure 27 and Figure 28 depict the size distribution for high loading and low rotational speed for MLRF1 graphite. The concentrations here are two orders of magnitude lower than those measured for the case of high loading and high rotational speed for the same material. The two tests yielded roughly similar concentration distributions with respect to time and both decrease steadily during the latter half of each test. In comparison to the same loading and rotational speed tests with commercial graphite, the concentrations are higher and are of a notably different shape in that they are much narrower.

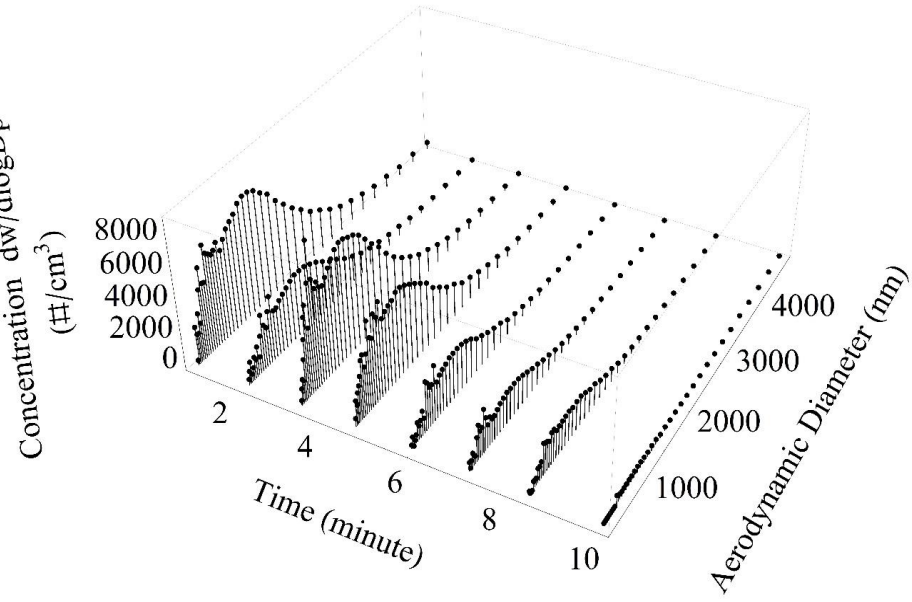

Figure 27. Particle size distribution for 48.93 kg and 450 rpm MLRF1 nuclear grade graphite. This graph has been corrected for background and represents test 11.

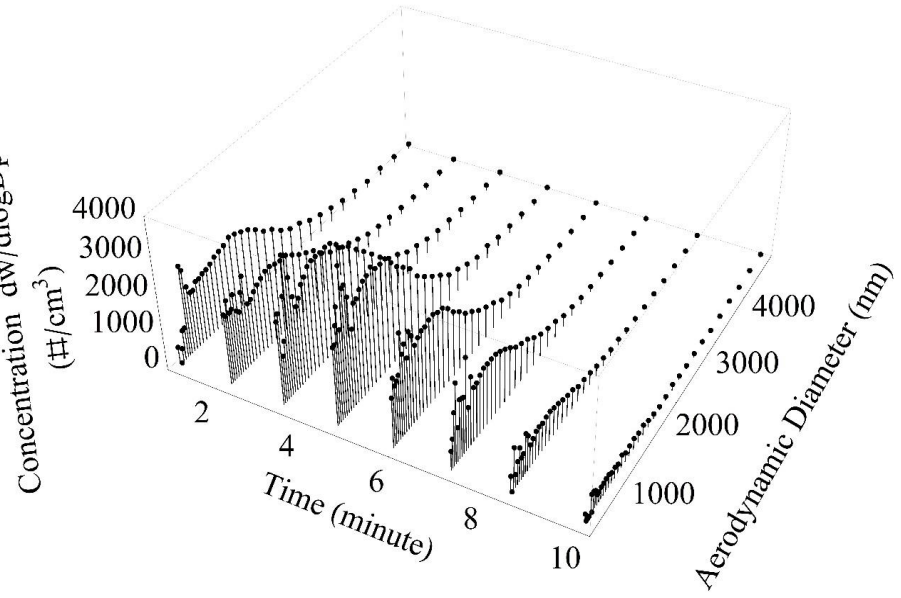

Figure 28. Particle size distribution for 51.27 kg and 450 rpm MLRF1 nuclear grade graphite. This graph has been corrected for background and represents test 12.

One common trend observed in all of the size distribution data from this work is that the nuclear-grade MLRF1 graphite yields increased particle concentrations that are more narrowly distributed than the distributions obtained in equivalent tests on the GM-101 commercial grade graphite. This observation is further supported by the wear rates (reported below) of the MLRF1 which are greater than those for the GM-101.

Dust that was deposited on pipes throughout the AVR reactor was scraped up, decontaminated, and de-agglomerated by ultrasonic treatment and then dried. Optical microscopy showed that the median number particle size was in the range of 0.2 to 0.7 μm whereas the median weight related size was in the range of 0.8 to 1.5 μm. It was also observed that dust adheres very strongly to the pipe walls.[26] The observed particle size in another AVR measurements was 1 μm or less.[27] From the IAEA TechDoc, "This number-weighted distribution indicates an average dust particle diameter of about 0.6 μm

which corresponds to a median diameter of about 5-10 µm for a particle volume weighted distribution. The size distribution of AVR dust seems to be similar for all filter experiments." [36] When you compare my measured size distributions in this work to the values cited above for the AVR, they appear to be in fairly good agreement.

As with all such particle sizing experiments, because of deposition in piping and apparatus, not all of my particles flow into the particle size measurement instruments. Since such deposited particles tend to form the larger heavier fractions, the reported resulting size distributions are thus not the true exact size distributions and are likely biased towards smaller size ranges. I recommend that before our data is used in computer simulations this fact be taken into account in some fashion. I conducted each test only twice as the results were similar for each repeated test. A larger number of tests would be certainly desirable for robustness of the data, but we believe the data reported here are quite typical of the results that would be obtained.

STATISTICAL ANALYSIS

I have fitted the measured size distributions with the expression from the TSI software, [11]

$$n(d_p) = \frac{A}{(\sqrt{2\pi}\ ln(C))} exp^{-\frac{1}{2}\left(\frac{ln\frac{d_p}{B}}{ln\,C}\right)^2} \qquad (8)$$

where, d_p is the particle aerodynamic diameter in and $n(d_p)$ is the assumed distribution as suggested by the data. *A*, *B*, and *C* are the fit parameters from Eq. 8 and are shown in Table 14. For each fit, I used experimental data from a certain data collection time during the test (relative to the starting point of the test). For some tests, particles were

only produced for a short time and, hence, fits have been generated for fewer times. Missing values simply represent where a distribution was not produced. The data collection proceeded in such a manner that data collection was integrated over one minute periods separated by 15 second intervals.

Missing tests in Table III, such as tests 5-8 and 9-12, represent tests were not enough particles were measured to appropriately fit distributions. The column labeled 'Goodness' is defined in the TSI Data Merge Software manual as a "Goodness of Fit" parameter that represents the average difference between the fitted size distribution and the data. The fitting algorithm determines the number of distribution functions to use and also determines the optimum fitting-function parameters for each distribution function by minimizing this "Goodness of Fit" parameter. The "Goodness of Fit" value tends to zero as the fit becomes perfect.

Test Number	Time (minute)	Goodness	Parameters		
			A	*B*	*C*
1	1.0	0.016	4320	8.56 E-7	1.93
	2.25	0.03	10700	8.34 E-7	1.89
	3.5	0.04	28200	8.08 E-7	1.72
	4.75	0.051	12400	7.1 E-7	1.87
	6.0	0.027	13100	7.5 E-7	1.83
	7.25	0.057	14800	7.31 E-7	1.84
	8.5	0.06	7030	7.68 E-7	1.85
	10.0	0.1	862	7.94 E-7	1.99
2	1.0	0.063	3770	7.49 E-7	2.11
	2.25	0.026	14200	7.62 E-7	2.09
	3.5	0.037	9610	7.78 E-7	2.06
	4.75	0.025	12600	8.1 E-7	1.85
	6.0	0.403	12000	8.14 E-7	1.83
	7.25	0.068	7620	8.17 E-7	1.92
	8.5	0.068	3.13 E6	6.82 E-8	2.06
	10.0	0.033	5.82 E5	3.14 E-8	2.19
3	1.0	0.019	3.83 E4	6.89 E-7	1.95
	2.25	0.027	6.93 E4	6.43 E-7	1.90
	3.5	0.032	9.09 E4	6.03 E-7	1.97
	4.75	0.031	1.53 E5	5.64 E-7	1.98
	6.0	0.04	1.83 E5	5.62 E-7	1.91
	7.25	0.045	1.31 E5	6.02 E-7	1.90
	8.5	0.049	1.58 E5	5.39 E-7	1.93
	10.0	0.16	1.13 E4	5.26 E-7	1.79
4	1.0	0.02	1.01 E5	6.48 E-7	1.96
	2.25	0.042	8.14 E4	5.86 E-7	1.90
	3.5	0.036	1.44 E5	5.92 E-7	1.92
	4.75	0.055	6.03 E4	5.69 E-7	1.92
	6.0	0.06	3.52 E5	5.89 E-7	1.82
	7.25	0.047	2.34 E5	5.68 E-7	1.90
	8.5	0.065	1.87 E5	5.41 E-7	1.84
	10.0	0.19	8.51 E3	5.38 E-7	1.77
9	1.0	0.0415	6.10 E2	8.29E-07	2.11
	2.25	0.0459	5.49 E2	7.98E-07	2.12
	3.5	0.0320	5.93 E2	8.51E-07	1.98
	4.75	0.0673	1.42 E3	9.15E-07	1.87
	6.0	0.0352	2.35 E3	8.47E-07	1.94
	7.25	0.0339	1.18 E3	7.71E-07	2.01
	8.5	0.0648	1.30 E3	8.19E-07	1.93
	10.0	N/A	N/A	N/A	N/A

	1.0	0.06	1.40 E3	8.71 E-7	2.05
	2.25	0.053	2.06 E3	8.58 E-7	2.04
	3.5	0.032	2.21 E3	8.42 E-7	2.05
10	4.75	0.044	2.20 E3	8.58 E-7	1.99
	6.0	0.022	1.91 E3	9.18 E-7	1.88
	7.25	0.077	1.18 E3	8.73 E-7	1.97
	8.5	0.066	1.46 E3	8.18 E-7	2.00
	10.0	N/A	N/A	N/A	N/A
	1.0	0.048	5.14 E3	7.26 E-7	1.90
	2.25	0.054	2.51 E3	7.33 E-7	1.84
	3.5	0.049	5.04 E3	6.64 E-7	1.85
11	4.75	0.024	3.93 E3	6.45 E-7	1.89
	6.0	0.053	1.84 E3	6.82 E-7	1.78
	7.25	0.071	1.37 E3	6.29 E-7	1.85
	8.5	0.021	1.26 E3	6.75 E-7	1.77
	10.0	0.174	2.91 E2	5.43 E-7	2.02
	1.0	0.042	1.38 E3	7.77 E-7	1.86
	2.25	0.049	1.73 E3	5.77 E-7	2.07
	3.5	0.055	2.21 E3	6.37 E-7	1.97
12	4.75	0.053	2.33 E3	6.21 E-7	1.90
	6.0	0.041	1.66 E3	6.38 E-7	1.84
	7.25	0.096	1.13 E3	6.88 E-7	1.78
	8.5	0.123	5.53 E2	6.46 E-7	1.84
	10.0	0.067	3.71 E2	4.06 E-7	2.57

Table 14. Fit Parameters from Eq. 8.

SHAPE AND SIZE FROM SEM ANALYSIS

To further characterize the generated particles and abraded surfaces, we used a Scanning Electron Microscope (SEM) to determine the shape of the particles. The points of contact were imaged for both the commercial GM-101 graphite and the nuclear-grade MLRF1 graphite and images were acquired both pre-abrasion as well as post-abrasion. I have shown the most representative images from our tests and those images can be seen in Figure 29 and Figure 30.

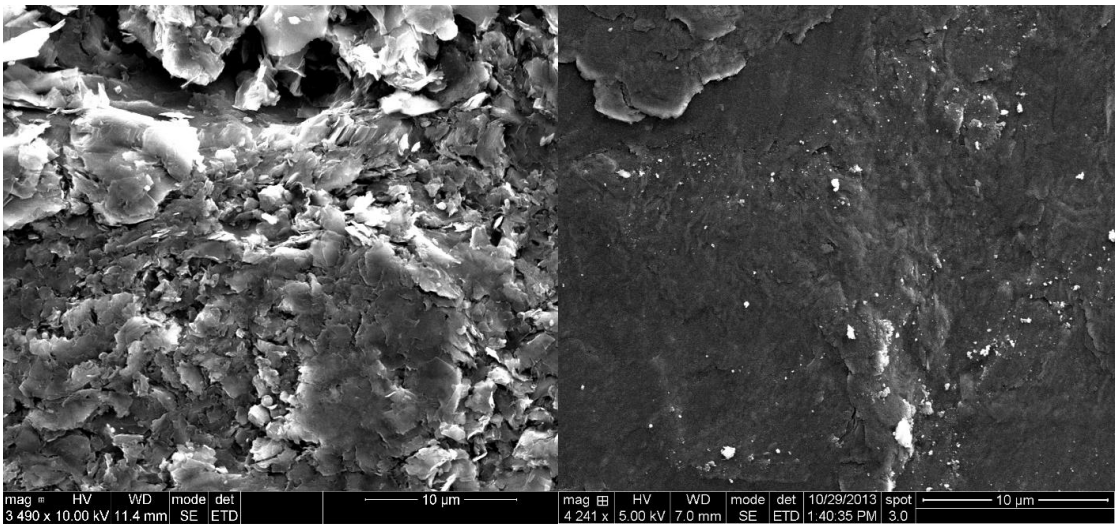

(a) (b)

Figure 29. SEM images of the surface where two commercial graphite samples made contact for the abrasion test: (a) before abrasion and (b) after abrasion from test 1.

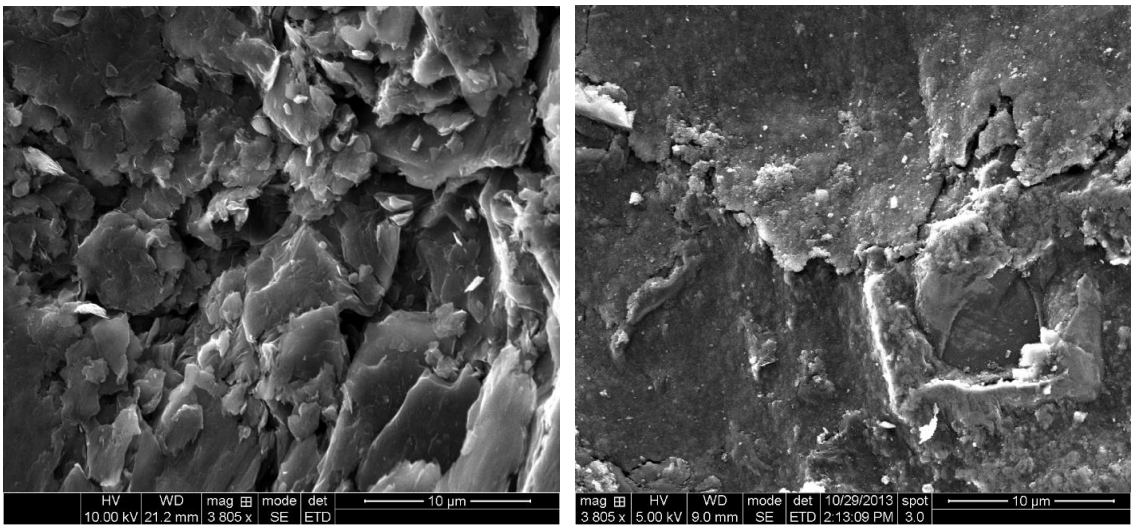

(a) (b)

Figure 30. SEM images of the surface where two MLRF graphite samples made contact for the abrasion test: (a) before abrasion and (b) after abrasion from test 3.

As one can see from Figure 29 and Figure 30, the surface of the graphite greatly changed after abrasion for both graphite types and this is further supported with the surface roughness data. As particles were generated, not all of them flowed into the APS and SMPS systems. The particles that settled on the chamber floor were collected and analyzed under SEM. I have shown some representative particle images from our tests. In current computer codes, particles are generally assumed to be spherical and my experiments show that is not a correct assumption as none of the particles in our testing are spheres. All of them have jagged edges and are irregular in shape. There is no consist shape between tests or particles within tests.

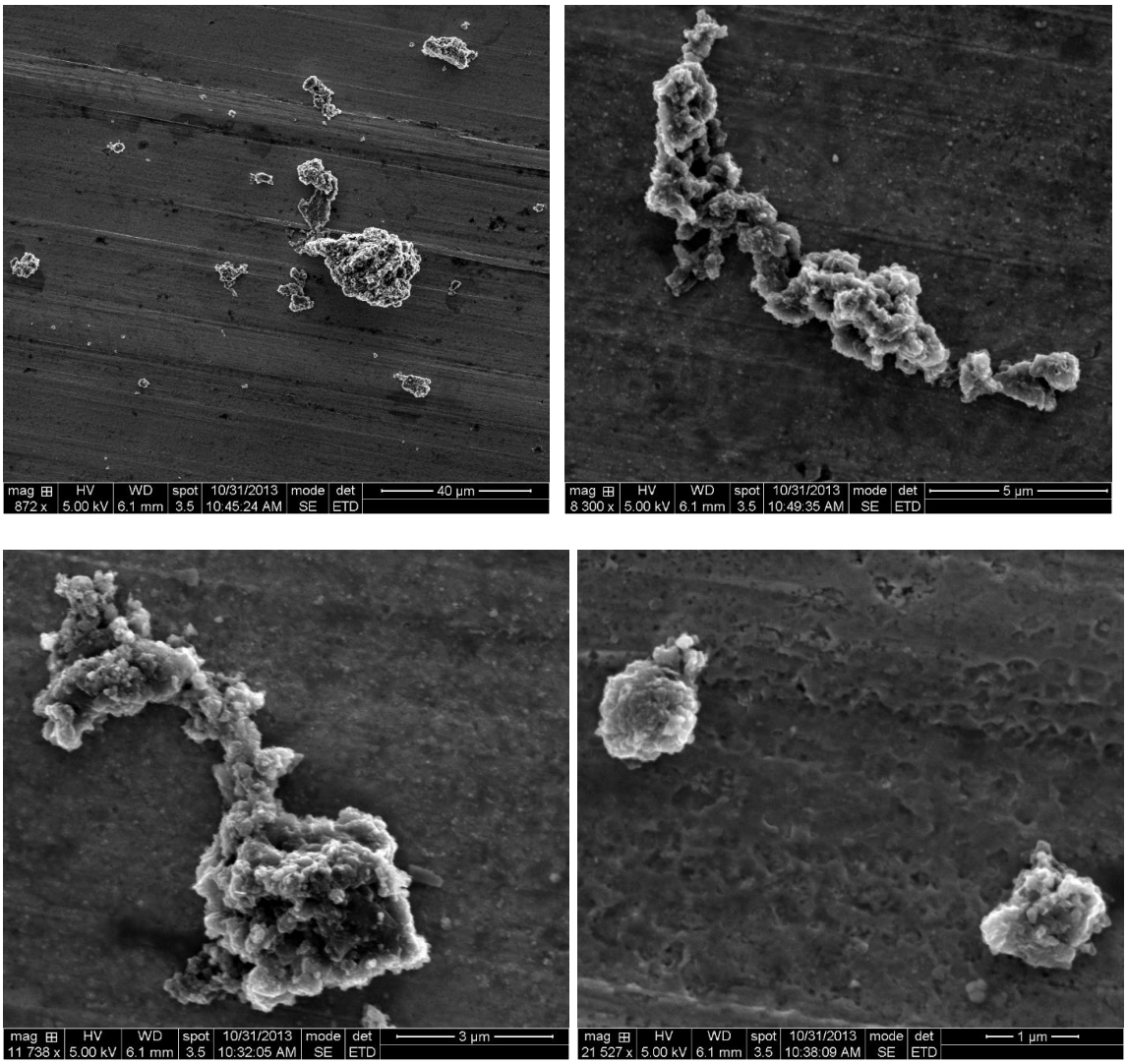

Figure 31. SEM micrographs of some typical dust particles that settled to bottom of the test chamber and were collected after abrasion between two commercial GM-101 graphite samples during test 1. Note the different SEM scale lengths from 1 µm (top left) to 40 µm (bottom right).

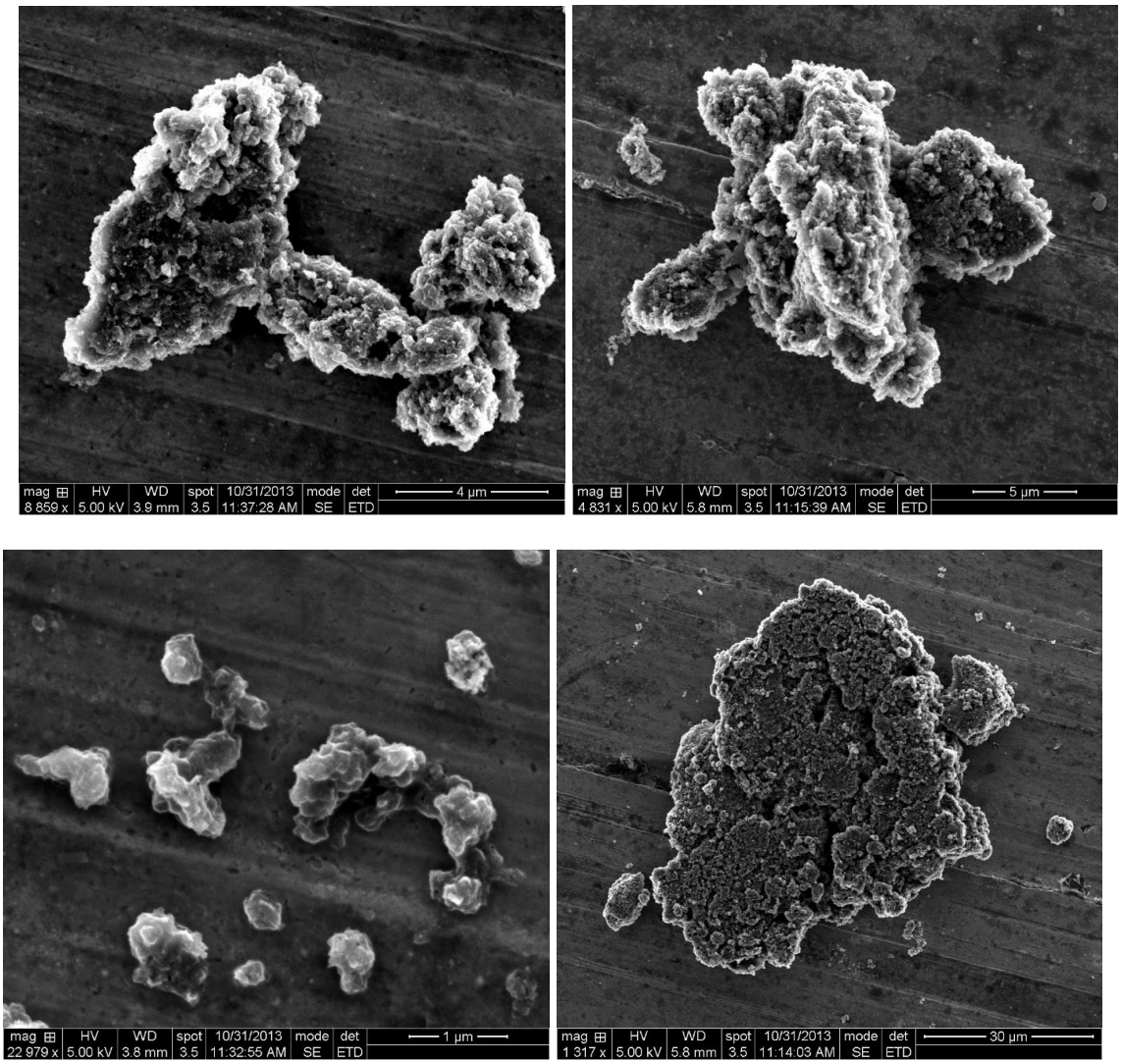

Figure 32. SEM micrographs of some typical dust particles that settled to bottom of the test chamber and were collected after abrasion between two nuclear grade MLRF1 graphite samples during test 3. Note the different SEM scale lengths from 1 µm (top left) to 30 µm (bottom right).

As one can see from Figure 31 and Figure 32, the particles are not round or spherical. Even though each type of graphite was made in a completely different way and each has very different bulk properties, it is difficult to distinguish between their abrasion particles by comparing either shape or size using SEM.

(a)

(b) (c)

(d)

(e) (f)

Figure 33. Photos of samples before (a, d) and after abrasion (b stationary sample, c rotated sample, e stationary sample, f rotated sample). (b,c) test 5. (e,f) test 3.

In Figure 33 you can see the samples wear patterns before abrasion and after. The test samples shown are from high load, high rotational speed tests 3 and 5. It is interesting to note the large difference between the two tests in terms of the contact points. The commercial grade wore in a more narrow and deeper crater than the MLRF1. In addition, the commercial displays a glassy surface while the MLRF1 is a dull surface.

BET SURFACE AREA, PORE VOLUME, AND POROSITY ANALYSIS

As particles were generated, some fell to the bottom of the test chamber and these were collected for SEM and BET surface area, pore volume, and pore size distribution analysis. The surface properties of the unabraded bulk graphites and four abraded graphite powder samples from tests 2, 3, 5, and 12 were characterized by BET N_2 isotherm adsorption at 77 K. The analysis was performed at Missouri University of Science and Technology using a Quantachrome® Autosorb IC instrument with ASiQwin data processing software. The N_2 isotherms for the four samples are shown in Figure 34.

It is observed that, as expected, the unbraided (bulk) graphite shows little nitrogen adsorption, indicative of a very low surface area, while the nitrogen adsorption increases significantly for the graphite dust particles collected during the sliding tests. N_2 adsorption isotherm data were analyzed using the quenched surface DFT (QSDFT) model assuming a slit/cylindrical pore geometry, to obtain the size distribution of open pores, the results are shown in Figure 35.

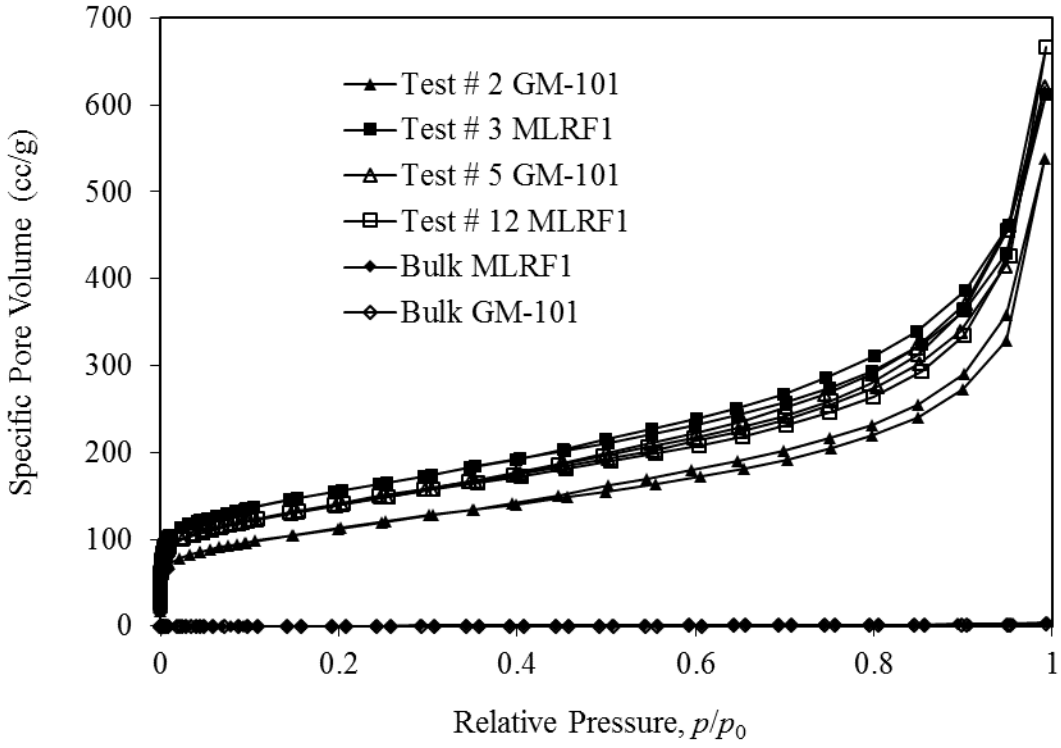

Figure 34. N2 isotherms for bulk graphite and dust samples produced during tests 2, 3, 5, and 12.

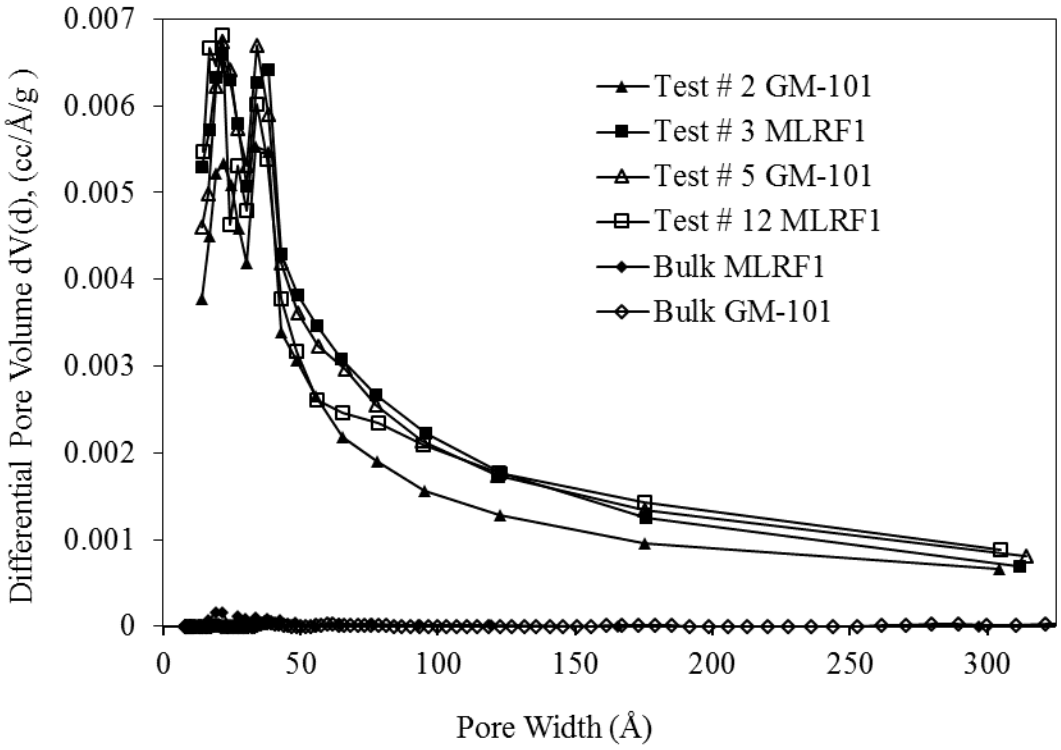

Figure 35. Pore size distributions for graphite dust particles produced during tests 2, 3, 5, and 12.

A summary of the results from the analysis of the N_2 isotherm data are shown in Table 15. It is observed that the surface area of the dust particles generated during the MLRF1 tests increases when the RPM is decreased from 1500 to 450 RPM while the loading is kept constant. For the commercial GM-101 graphite, the surface area increases when the loading decreased from 51.51 kg to 17.24 kg and RPM stayed constant at 1500 RPM. This porosity within the particles is of great interest, since it could serve as means for adsorption of fission products, and would represent a significant safety issue if released. For comparison of these surface area measurements to both my previous work and additional works please see my previous work.[35]

	BET Surface Area ($m^2\ g^{-1}$)*	Total Pore Volume ($cm^3\ g^{-1}$)*
Unabraded (bulk) commercial graphite	0.58	0.006
Unabraded (bulk) MLRF graphite	2.78	0.004
Abraded graphite Test # 2 (commercial)	398	1.021
Abraded graphite Test # 3 (MLRF)	545	1.272
Abraded graphite Test #5 (commercial)	493	0.854
Abraded graphite Test #12 (MLRF)	490	0.886

Table 15. Surface properties of graphite samples.

* Data from nitrogen adsorption at 77 K. The BET surface area is calculated using the Brunauer - Emmett - Taylor equation. The total pore volume is measured at maximum nitrogen pressure.

The multipoint Brunauer-Emmett-Teller (BET) method was used to determine the surface area of the particles. BET surface area is obtained using the equation:

$$W^{-1}\left(\frac{p_0}{p}-1\right)^{-1}=\frac{1}{W_m C}+\frac{C-1}{W_m C}\left(\frac{p}{p_0}\right) \tag{9}$$

where W is the weight of the gas adsorbed at a relative pressure, p/p_0, W_m is the weight of adsorbate constituting a mono layer of surface coverage, and C is a constant. In the BET method, a plot of $W^{-1}\left(\frac{p_0}{p}-1\right)^{-1}$ vs. p/p_0 in the range of $0.05 \le p/p_0 \le 0.35$, which is referred to as the range for monolayer coverage, yields a straight line. The slope of this line, S, and its intercept, i, are given by:

$$S = \frac{C-1}{W_m C} \tag{10}$$

and:

$$i = \frac{1}{W_m C} \tag{11}$$

Using Eqs. (3) and (4), the monolayer coverage W_m is simply:

$$W_m = \frac{1}{S+i} \tag{12}$$

The total surface area, S_t, can, therefore, be obtained as:

$$S_t = \frac{W_m N A_{CS}}{M} \tag{13}$$

where A_{CS} is the cross-sectional area of the adsorbate molecule which, for nitrogen, is 16.2 Å^2, N is Avogadro's number, and M is the molecular weight of the adsorbate. Then, one has the specific surface area of the solid, S_{SP}, given by:

$$S_{SP} = \frac{S_t}{W} \tag{14}$$

SURFACE ROUGHNESS MEASUREMENTS

With each graphite studied, the surface roughness was measured on three different bulk samples before abrasion and an average was taken. After abrasion, surface roughness was again measured on the test samples across the contact point of both the top and bottom halves. In our analysis of the surface roughness, we used four quantities to characterize surface roughness in accordance with the work of Bushan [31]. Here, y_i

simply represents the heights (positive or negative) of an array of measured points within some evaluation area on the sample relative to the average height. The surface roughness R_a of Eq (15) is then just the average magnitude of the height calculated over the entire evaluation area involving a total of n measured points. Similarly, R_q of Eq. (16) is the root-mean-squared roughness calculated over the entire evaluation area involving a total of n measured points. R_v and R_p of Eqs. (17) and (18) are the low (valley) and high (peak) points measured in the evaluation area, respectively, and are used to determine the adjacent peak-to-valley differences R_t of Eq. (19) for points in the evaluation area. Finally, R_z is the ten-point height. This is the average of the ten greatest peak-to-valley differences detected across the evaluation area as indicated in Eq. (20).

$$R_a = \frac{1}{n}\sum_{i=1}^{n}|y_i| \tag{15}$$

$$R_q = \sqrt{\frac{1}{n}\sum_{i=1}^{n}y_i^2} \tag{16}$$

$$R_v = \min\left(y_i\right) \tag{17}$$

$$R_p = \max\left(y_i\right) \tag{18}$$

$$R_t = R_p - R_v \tag{19}$$

$$R_z = \frac{1}{10}\sum_{i=1}^{10}\max\left(R_{t,i}\right) \tag{20}$$

A table of these values can be seen below in Tables 17-19.

Sample Number	Ra (µm)	Rq (µm)	Rz (µm)	Rt (µm)
101	8.91	11.92	83.4	92.65
102	2.42	3.2	28.44	37.2
103	1.94	2.6	25.58	34.22
Average	4.42	5.91	45.81	54.69

Table 16. Surface Roughness of Pre-abraded Samples of Commercial GM-101 Graphite at 2.5×.

Sample Number	Ra (µm)	Rq (µm)	Rz (µm)	Rt (µm)
121	3.07	4.3	46.63	59.87
122	5.58	9.87	133.35	172.1
123	3.54	6.15	83.17	132.43
Average	4.06	6.77	87.72	121.47

Table 17. Surface Roughness of Pre-abraded Samples of Nuclear-grade MLRF1 Graphite at 2.5×.

Sample Number	Ra (µm)	Rq (µm)	Rz (µm)	Rt (µm)
127 5×	1.11	1.98	88.80	122.83
127 50×	0.23	0.30	6.94	11.54
127 5×	7.86	12.01	264.01	311.91
127 50×	0.62	0.79	28.89	52.02
127 5×	4.84	7.47	210.70	268.26
127 50×	1.04	4.59	256.10	296.74

Table 18. Surface Roughness of Pre-abraded Sample 127 of Nuclear-grade MLRF1 Graphite at 5× and 50×.

Test Number	Sample Number	Location	Ra (µm)	Rq (µm)	Rz (µm)	Rt (µm)	Driver
1	101	A	24.44	32.8	461.85	481.71	N
1	101	B	2.47	7.34	280.6	302.23	N
1	101	C	1.65	5.01	255.26	292.23	N
1	101	D	1.56	5.69	237.38	303.79	N
1	102	A	85.06	107.39	1158	1208	Y
1	102	B	2.98	7.842	202.36	206.5	Y
1	102	C	9.55	17.48	212.4	215.9	Y
1	102	D	0.952	3.895	191.1	199	Y
2	103	A	33.39	44.46	760.35	870.51	N
2	103	B	3.08	7.54	278.48	302.94	N
2	103	C	8.88	17.88	298.99	303.45	N
2	103	D	0.33	1.34	153.59	246.51	N
2	104	B	5.453	11.91	211.4	217.4	Y
2	104	C	4.895	11.18	230.1	240.7	Y
2	104	D	1.328	2.339	175.5	197.1	Y
13	113	A	74.86	92.41	631.32	655.94	N
13	113	B	7.03	17.28	290.67	298.48	N
13	113	C	12.17	21.95	306.85	324.68	N
13	113	D	12.05	22.72	299.81	313.69	N
13	114	A	11.19	16.49	342.06	378.20	Y
13	114	B	17.64	29.72	293.30	311.07	Y
13	114	C	23.44	35.45	297.92	310.99	Y
13	114	D	6.07	14.96	300.85	306.60	Y
14	115	A	29.78	37.69	374.25	383.59	N
14	115	B	17.77	29.64	302.80	315.47	N
14	115	C	6.67	16.13	300.47	309.09	N
14	115	D	15.60	27.41	296.83	317.23	N
14	116	A	11.78	18.68	301.08	315.13	Y
14	116	B	11.52	23.51	296.91	318.00	Y
14	116	C	7.32	16.71	291.76	309.49	Y
14	116	D	8.31	18.82	273.85	295.61	Y

Table 19. Surface Roughness of Abraded Commercial GM-101 Graphite Samples

Test Number	Sample Number	Location	Ra (µm)	Rq (µm)	Rz (µm)	Rt (µm)	Driver
3	120	A	24.47	30.26	363.01	374.97	N
3	120	B	1.51	3089	247.70	296.95	N
3	120	C	6.38	15.70	297.69	301.73	N
3	120	D	4.26	11.69	287.69	301.73	N
3	121	A	5.48	13.53	314.60	334.60	Y
3	121	B	2.35	8.07	286.94	302.54	Y
3	121	C	16.01	25.66	303.52	310.98	Y
3	121	D	3.26	10.38	288.13	302.35	Y
4	122	A	35.03	44.99	350.05	361.36	N
4	122	B	14.28	25.85	299.20	304.97	N
4	122	C	6.06	13.50	293.68	303.85	N
4	122	D	7.12	15.37	296.93	305.95	N
4	123	A	45.42	55.50	355.91	366.24	Y
4	123	B	6.06	13.46	298.75	305.13	Y
4	123	C	11.86	20.41	302.42	311.28	Y
4	123	D	10.94	20.69	305.25	316.72	Y
15	124	A	11.17	14.31	311.67	348.95	N
15	124	B	1.72	5.59	255.11	290.23	N
15	124	C	5.94	14.93	296.15	303.77	N
15	124	D	1.01	5.16	252.05	289.75	N
15	125	A	12.4	16.24	315.28	353.28	Y
15	125	B	16.87	29.47	321.47	339.73	Y
15	125	C	9.19	18.13	300.77	306.29	Y
16	126	A	5.97	8.20	275.09	302.65	N
16	126	B	3.22	8.96	284.54	297.78	N
16	126	C	0.96	5.04	291.91	305.59	N
16	126	D	0.66	4.55	247.06	284.51	N
16	127	A	4.50	7.16	282.20	305.23	Y
16	127	B	1.26	4.30	167.88	241.77	Y
16	127	C	6.14	13.89	285.24	298.65	Y
16	127	D	0.76	2.09	162.63	241.67	Y

Table 20. Surface Roughness of Abraded Nuclear-Grade MLRF1 Graphite Samples

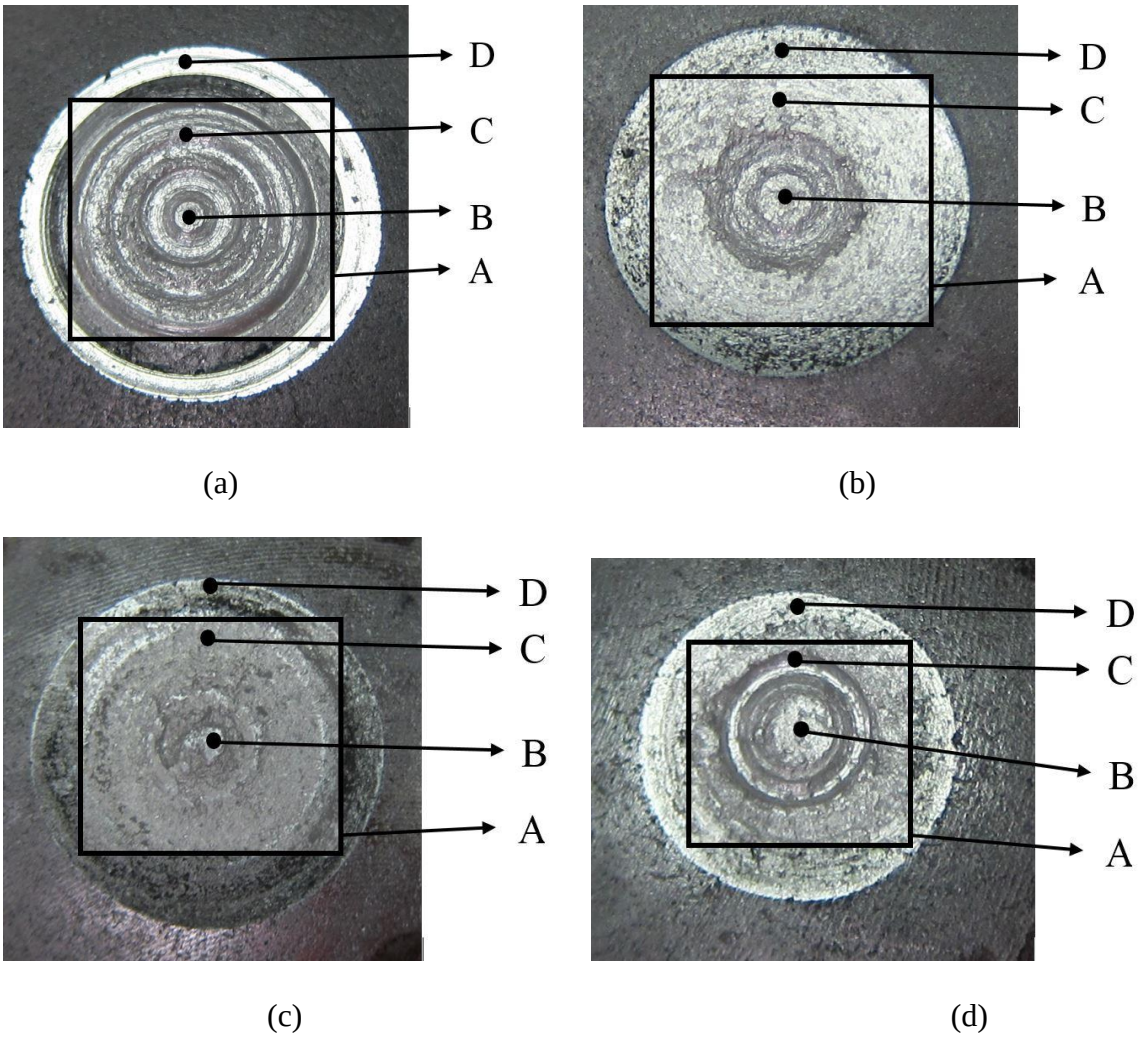

Figure 36. Depiction of surface roughness measurement points considered. (a) sample 101, (b) sample 113, (c) sample 121, (d) sample 125. Surface sampling areas indicated by A represent a zoom setting on the Wyko® NT9100 of 2.5× while areas indicated by B, C, and D represent a zoom setting of 50×. The lower the zoom setting, the greater the measurement area.

The Wyko® NT9100 has four different zoom settings 2.5×, 5×, 20× and 50× to change the area measured. For the sample area A the largest, 2.5× was used and for B, C, and D, the smallest, 50× was used. We have found that surface roughness is very location specific and can vary from location to location as well as within a given measurement area. In general, but not as a rule, the smaller sampling areas (20×, 50×) have lower overall surface roughness. The surface roughness is a very local property.

When obtaining the surface roughness measurements on very small areas (high magnification), an adjacent area can have a very different value. The inclusion of the surface roughness data is meant to show this strong dependence on location and that it is not an inherent consequence of abrasion. The measurements are believed to be accurate but the strong dependence on the area selected can give a surface roughness that is not indicative of the entire sample. We are unable to provide an error analysis because of the nature of the Wyko instrumentation that we used.

HUMIDITY AND TEMPERATURE

Throughout testing, humidity and temperature was measured inside the test chamber for references purposes only. There was no effort made to precisely control either the relative humidity or the chamber temperature. However, low humidity air was used in all of the tests to help achieve the dusting effect.[24, 25, 8] This low humidity air was introduced at 12 L min^{-1} into the test chamber which drove humidity to levels below about 5.5% in every test. Since humidity was not one of the critical variables being studied in this work, only one representative humidity plot has been presented and is shown in Figure 37 which is specific to test five (53.9 kg loading and 450 rpm) and is the test that exhibited the largest observed variation in relative humidity during testing. As one may see from Figure 37, the relative humidity decreases in the latter half of the test which is typical of all the tests and seems likely due to the increasing temperatures in the test chamber which occurred during every test. The specific minimum, maximum, and average relative humidity values observed in each test are given in

Table 21.

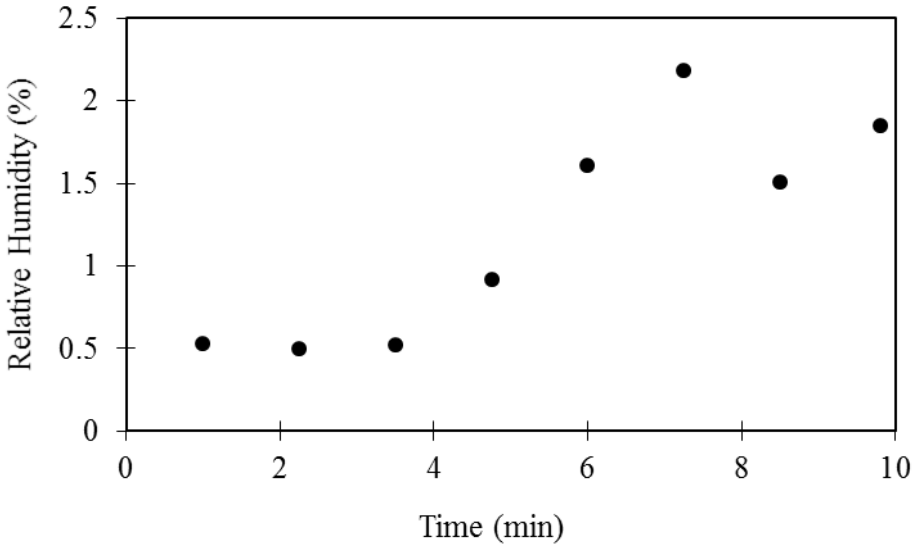

Figure 37. Representative plot of the humidity inside the test chamber during testing. This was from test 5 (53.9 kg and 450 rpm). This is a typical plot in that the relative humidity decreases in the latter half of the test which we believe is due to the temperature increasing throughout the test.

Test Number	Max	Min	Average
1	2.27	0.49	1.27
2	2.36	0.49	0.91
3	5.46	1.65	3.5
4	1.23	0.61	0.90
5	0.76	0.56	0.67
6	0.99	0.69	0.78
7	3.10	0.62	1.49
8	0.95	0.61	0.73
9	0.78	0.56	0.65
10	0.68	0.52	0.61
11	2.19	1.92	2.00
12	1.71	1.46	1.54
13	0.55	0.34	0.44
14	0.74	0.51	0.63
15	1.49	1.25	1.36
16	1.39	1.63	1.54

Table 21. Relative Humidity Values Measured During Abrasion Testing.

In addition to the chamber temperature being measured, after all 16 test runs were completed, we carried out one more test run to obtain the temperature at the surface at one of the points of contact. I attached four thermocouples very close to the point of abrasion, to the stationary sample and these results are shown in Figure 38.

The loading for the 56 kg, 1500 rpm MLRF1 test was decreased for 2 minutes due to heavy chattering starting near minute 3. I do not think the temperature would have exceeded the 160 °C temperature observed during the corresponding GM-101 test. As one can see from the initial slope of the 56 kg, 1500 rpm MLRF1 test it was below the same loading and rotational speed for the GM-101 and we would estimate the value of the temperature to be around 130 °C at its peak if loading had not been reduced. I did not feel that the experiment needed to be repeated due to this anomaly.

The surface temperature has an effect on the wear mechanism. Lancaster[24] states that a transition to dusting occurs in the range of 150-200 °C at the contact surface in atmospheric air (50% humidity). Due to my lower humidity environment and the large particle production for high loading (both high and low rotating speeds), I believe that the dusting regime has been achieved. For the lower loading, I am not as confident that dusting has been achieved for two reasons. First, the amount of heat production is low as evidenced by the chamber temperature plots below, indicating a low surface contact temperature. Second, the amount of particle production is low. Due to the particle production and heat produced we can safely state that we are in the dusting regime for each of the high loading experiments. While we did not reach the 150-200 °C contact temperature that has been observed in the past, dusting was achieved by the low relative humidity and the temperatures of the surfaces of the samples.

Lancaster[25] also states the saturation pressure (which is related to contact and environmental temperature), loading and sliding speed (which are related to contact temperature and heat generation) influence in the transition to dusting. In addition, since for each test the results are very similar and the humidity values slightly differed for each test, then dusting was not affected by the small change in humidity. I am not able to predict if there is a transition to a dusting regime due to humidity in the humidity range of my experiments.

Yen, et al.[8], conducted experiments in nitrogen and air with a low-speed three-pins-on-disc apparatus and a high-energy ring-on-ring apparatus. They made their own carbon-carbon composite material which contained 40% fiber, 47% matrix, and 13% porosity. The humidity for the tests was measured to be between 100 ppm to 50 % RH for both working gases, air and nitrogen. They also observed that dusting is dependent on sliding distance, contact pressure and sliding speed mainly through their influence on contact surface temperature.

In regards to temperature, Figure 39 is very representative plot. Temperature always increases throughout each of the tests with the largest increase observed in test 5 (53.9 kg and 450 rpm). This great increase in temperature is expected as this is the highest loading and highest rotational speed tested which would indicate the most friction. It was surprising just how much heat was generated. In test 5 generated heat was sufficient to produce a 20.98 °C difference from ambient. This must represent a significant heat production as there is certainly convective cooling occurring from the 12 L min−1 low humidity air flow. One would also expect that as temperature increases during each test relative humidity would decrease and this is what was observed in all the

tests. As loading and/or rpm decreased so did the heat produced which is also what one would expect.

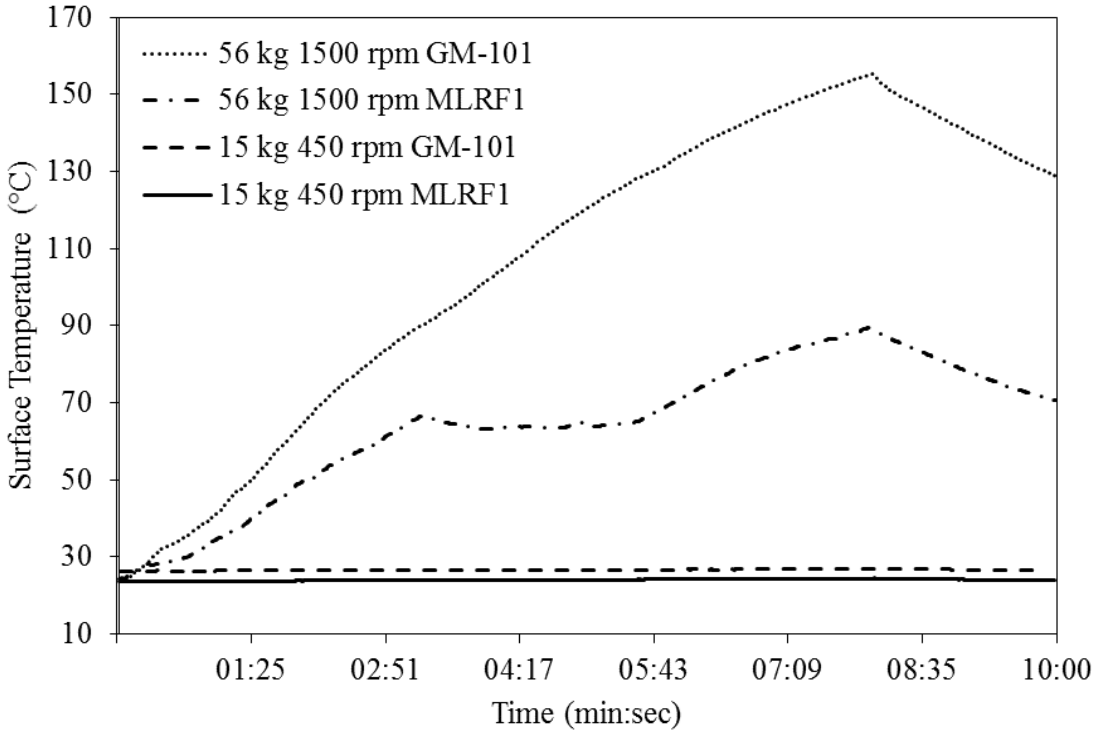

Figure 38. Surface temperature of samples.

The loading for the 56 kg 1500 RPM MLRF test was decreased for 2 minutes due to heavy chattering starting near minute 3. We do not think the temperature would have exceeded the commercial test of 160 °C. As one can see from the initial slope of the 56 kg 1500 RPM MLRF test it was below the same loading and rotational speed for commercial and we would estimate the value of the temperature to be around 130 °C at its peak if loading had not been reduced. We did not repeat the experiment due to the high cost of the materials.

In regards to chamber temperature, Figure 39 is very representative plot. Temperature always increases throughout each of the tests with the largest increase in test

number five (53.9 kg and 450 RPM). This great increase in temperature is expected as this is the highest loading and highest rotational speed tested which would indicate the most friction. It is surprising at just how much heat is generated, in this test there is a 20.98 degree difference. There is significant heat produced as keep in mind there is convective cooling occurring from the 12 L m^{-1} low humidity air flow. One would also draw the conclusion that as temperature increased humidity decreased which is what is observed in all the tests. As loading or RPM decreased so did the heat produced, which is expected.

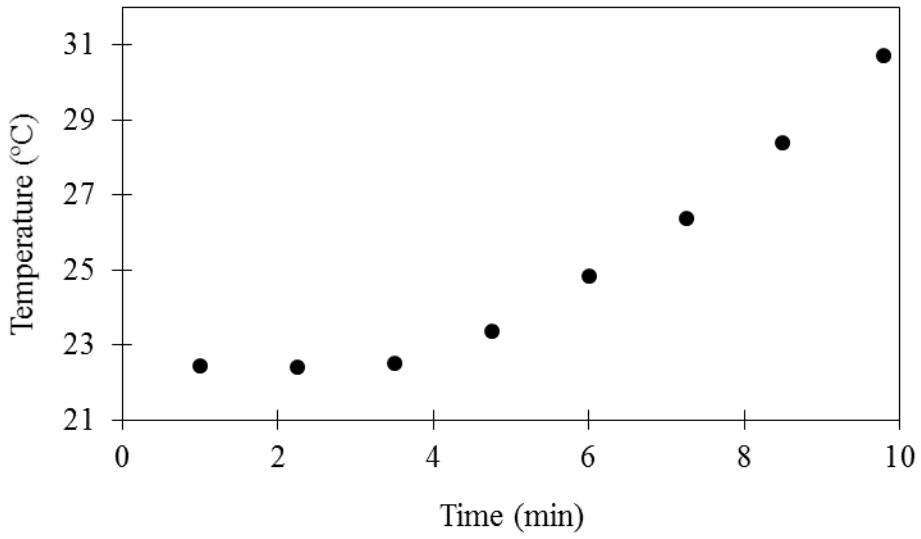

Figure 39. Representative Plot of Temperature inside test chamber during testing. This was from test 5 (53.9 kg and 450 RPM).

Test Number	Max (°C)	Min (°C)	Average (°C)
1	32.11	22.42	25.90
2	34.36	24.67	27.73
3	36.65	24.19	28.73
4	36.93	26.34	30.91
5	24.53	22.10	22.97
6	25.42	23.36	24.19
7	26.28	23.45	24.68
8	25.33	22.95	24.03
9	25.89	22.44	23.69
10	26.28	23.62	24.61
11	24.53	23.35	23.79
12	23.97	22.17	22.82
13	24.77	23.91	24.15
14	24.42	23.93	24.10
15	23.76	23.32	23.52
16	23.32	23.24	23.27

Table 22. Temperature Values Measured During Abrasion Testing

WEAR RATE

One desirable quantity to be determined for graphite that is being abraded is wear rate. As one can see from Table 23, as the loading or rpm increased among the various tests so did the wear rate. After visually inspecting the samples after testing, it came as no surprise that the quantitative mass measurements showed that the samples being driven by the milling machine (as opposed to those that were fixed) generally lost the most mass. With each repetition of each test the total mass loss values were of the same order magnitude as in the first test and this signifies that graphite abrasion process, overall, is not as chaotic and unpredictable as one might think provided that the time frame for the abrasion is sufficiently long. One must also be cautious of these wear rates as they are not measured at each sampling time but are averaged over the whole test. In

some tests, particles were not produced the entire time but the total mass loss was divided by the total time.

There is very little previous work that has been performed on spinning abrasion and, hence, comparing our observed wear rates to previous work is difficult. One can, potentially, attempt to compare these results to other works on sliding abrasion referenced in our previous work.[35] It is, however, difficult to make these comparisons as previous values have generally been reported in units of mass per length.

Test Number	Sample Number	Starting Mass (g)	Ending Mass (g)	Mass Difference (g)	Total Mass Loss (g)	Wear Rate Per Sample (g/min)	Total Wear Rate (g/min)	Driven
1	101	194.7772	194.6990	0.0782	0.1661	0.0098	0.0208	No
	102	190.0646	189.9767	0.0879		0.0110		Yes
2	103	186.5990	186.5031	0.0959	0.4281	0.0120	0.0535	No
	104	189.8110	189.4788	0.3322		0.0415		Yes
3	120	196.8827	196.6349	0.2478	0.5260	0.0310	0.0658	No
	121	197.5481	197.2699	0.2782		0.0348		Yes
4	122	198.2182	198.0010	0.2172	0.5588	0.0271	0.0698	No
	123	196.6382	196.2966	0.3416		0.0427		Yes
5	109	197.5199	197.4834	0.0365	0.052	0.0046	0.0065	No
	110	193.2998	193.2843	0.0155		0.0019		Yes
6	107	194.4690	194.4459	0.0231	0.0413	0.0029	0.0052	No
	108	192.9849	192.9667	0.0182		0.0023		Yes
7	120	196.9085	196.8812	0.0273	0.0564	0.0034	0.0070	No
	121	197.5748	197.5457	0.0291		0.0036		Yes
8	122	198.2611	198.2207	0.0404	0.0694	0.0051	0.0087	No
	123	196.6695	196.6405	0.0290		0.0036		Yes
9	105	192.0969	192.0032	0.0937	0.1661	0.0117	0.0208	No
	106	194.7192	194.6468	0.0724		0.0090		Yes
10	111	194.0198	193.9823	0.0375	0.1453	0.0047	0.0182	No
	112	196.6120	196.5042	0.1078		0.0135		Yes
11	124	198.2669	198.2098	0.0571	0.1004	0.0071	0.0126	No
	125	198.1311	198.0878	0.0433		0.0054		Yes
12	126	197.5940	197.4907	0.1033	0.1476	0.0129	0.0184	No
	127	196.8296	196.7853	0.0443		0.0055		Yes
13	113	191.9838	191.9652	0.0186	0.0241	0.0023	0.0030	No
	114	194.1899	194.1844	0.0055		0.0007		Yes
14	115	185.7784	185.7494	0.0290	0.0345	0.0036	0.0043	No
	116	195.2001	195.1946	0.0055		0.0007		Yes
15	124	198.2834	198.2661	0.0173	0.0281	0.0022	0.0035	No
	125	198.1404	198.1296	0.0108		0.0013		Yes
16	126	197.6059	197.5938	0.0121	0.0222	0.0015	0.0028	No
	127	196.8397	196.8296	0.0101		0.0013		Yes

Table 23. Wear Rate.

CONCLUSIONS

I have generated size distributions for the abraded particles, fit lognormal functions to those size distributions (for use in computer codes), determined particle shapes, measured temperature and humidity in the chamber during the tests, measured surface temperatures, calculated wear rates, measured the surface roughness pre and post-test, particle surface areas, pore volumes, and pore volume distributions of particles produced during abrasion of graphites surfaces under different loadings and rotational speeds.

The particle size distributions and concentrations were effected by loading and rotational speed. As the loading and rotational speed increased so did the concentration of particles generation. The observed distributions generally involved particles with sizes <4000 nm for the commercial GM-101 graphite and <~3000 nm for the nuclear grade MLRF1 graphite. Generally, the distributions tended to peak somewhere in the range of 1000-1500 nm for both types of graphite. As the loading and sliding speed increased so did the concentration. Maximum concentrations generally occurred somewhere between 2-6 min into the test which likely represents some optimum condition for abrasion being reached in terms of total load and abraded area. It is interesting with that in these tests of spinning abrasion, the similarities in the repeated tests are apparently not as strong as seen in our work on sliding abrasion[5]. This seems likely to be due to some type of structural inhomogeneity within the graphite that was randomly encountered during the test. Such may be important, however, given the large number of particles generated when they occur. Lognormal statistical fits to the observed distributions should be useful in computer codes in the future for predicting various needed values. I also note that

there was no “break in period” as seen in my earlier work as particle production started immediately in every test. I feel this is due to the low humidity atmosphere that was used. Somewhat different from our previous work, this work tended to generate a large amount of particles in a shorter period of time. Overall, the particle generation in this work appears fairly consistent except in the one case where the large particle burst occurred. The nuclear grade MLRF1 graphite has the characteristics of a softer graphite as it has consistently higher concentrations of particles produced. In addition, the range of sizes of particles produced is smaller with the nuclear MLRF1 graphite. This may be due to the size of particles from which each graphite is originally produced.

The particles generated are not spherical as seen in the SEM images. The particles that were viewed under SEM were ones that had fallen to the bottom of the test chamber and, thus, there may be bias. These particle may have been too large or heavy to be carried to the particle sizers. The surfaces of the samples are greatly changed during abrasion as seen from the SEM images. To the naked eye the post abrasion samples look much smoother and almost glassy and shiny with the GM-101 graphite and smooth and dull with the MLRF1. The samples at higher loading and rotation have rings on them where the abrasion was constant for some period of time and then increased causing a new ring. This process was repeated several times but does not appear to be particularly reflected in the size distributions. In addition, the size of the wear sites was observed to depend greatly on loading and rotational speed.

It was found that significant surface area and porosity are created within the dust particles and that the surface area increases with loading. The mechanism by which the large porosity is created is not completely understood, however, it merits more attention

and further investigation since this can strongly affect partitioning of fission products in the gas phase, surfaces and the dust, affecting overall transport of fission products.

There is a significant amount of heat that is produced during these tests especially at the high loading and rotational speeds, even as the convective forces of the low humidity air are cooling the chamber. I was successful in maintaining a low humidity environment for all the tests and further testing should be done in different environments. No attempt was made to regulate humidity to a specific value or maintain or elevate temperature. Even though I did not try to regulate these values I feel they are important to report. Due to the dust flowing directly into our testing equipment, I cannot perform tests in an elevated temperature testing configuration without making significant system modifications. In addition to measuring the temperature of the chamber, after the initial 16 tests were completed we conducted four additional tests to measure the surface temperatures as this likely has a significant effect on reaching the dusting regime or not.

As loading and rotational speed increased so did wear rate. This is to be expected as additional forces abrade the graphite and take material off the sample. Please keep in mind that wear rate was calculated using mass loss measured from the beginning to the end of the tests unlike has been done in some other works.

The present work suggests future tests on different graphite types and grades under a range of controlled environments should continue. Different shapes of the interacting graphites should be tested for comparison with this and previous works. There is, in particular, a clear need to elucidate mechanisms that lead to such large intra-particle porosities and surface areas in the abraded particles, and there is also an ongoing

need to verify particle generation, evolution and transport modeling results against experimental data.

REFERENCES

1. C. C. STOKER, L. D. OLIVIER, E. STASSEN, F. REITSMA AND J. J. VAN DER MERWE, "PBMR radionuclide source term analysis validation based on AVR operating experience," *Nuclear Engineering and Design.* 240, 10, 2466-2484, (2010).

2. M. P. KISSANE, F. ZHANG AND M. W. REEKS, "Dust in HTRs: Its nature and improving prediction of its resuspension," *Nuclear Engineering and Design.* 251, 301-305, (2012).

3. M. M. STEMPNIEWICZ, L. WINTERS AND S. A. CASPERSSON, "Analysis of dust and fission products in a pebble bed NGNP," *Nuclear Engineering and Design.* 251, 433-442, (2012).

4. M. ROSTAMIAN, G. JOHNSON, M. HIRUTA, G. P. POTIRNICHE, A. M. OUGOUAG, J. J. COGLIATI AND A. TOKUHIRO, "Computational and experimental prediction of dust production in pebble bed reactors-Part I," *Nuclear Engineering and Design.* (2013).

5. M. ROSTAMIAN, G. P. POTIRNICHE, J. J. COGLIATI, A. OUGOUAG AND A. TOKUHIRO, "Computational prediction of dust production in pebble bed reactors," *Nuclear Engineering and Design.* 243, 33-40, (2012).

6. A. G. POLSON, "Distinct element method analyses of fuel spheres in the PBMR core using RFC3D," 2004, (2004).

7. W. PENG, Y. ZHEN, X. YANG AND S. YU, "Graphite dust deposition in the HTR-10 steam generator," *Particuology.* 11, 5, 533-539, (2013).

8. B. K. YEN, T. ISHIHARA AND I. YAMAMOTO, "Influence of environment and temperature on "dusting" wear transitions of carbon-carbon composites," *Journal of Materials Science.* 32, 3, 681-686, (1997).

9. F. ROBERT, D. PAULMIER, H. ZAÏDI AND E. SCHOULLER, "Combined influence of an inert gas environment and a mechanical action on a graphite surface," *Wear.* 181-183, PART 2, 687-690, (1995).

10. D. H. BUCKLEY AND W. A. BRAINARD, "Friction and wear of metals in contact with pyrolytic graphite," *Carbon.* 13, 6, 501-508, (1975).

11. C. C. LI AND J. E. SHEEHAN, "FRICTION AND WEAR STUDIES OF GRAPHITE AND A CARBON-CARBON COMPOSITE IN AIR AND IN HELIUM," *Wear of Materials: International Conference on Wear of Materials.* 525-533, (1981).

12. K. KIKUCHI, H. KABURAKI, K. SANOKAWA, K. KAWAGUCHI, M. NEMOTO AND S. WATANABE, "IMPURITY GAS EFFECTS ON FRICTION AND WEAR OF HIGH-TEMPERATURE MATERIALS FOR VHTRs," *Nuclear Technology.* 66, 3, 491-502, (1984).

13. J. C. RIETSCH, R. GADIOU, C. VIX-GUTERL AND J. DENTZER, "The influence of the composition of atmosphere on the mechanisms of degradation of graphite in planetary ball millers," *Journal of Alloys and Compounds.* 491, 1-2, L15-L19, (2010).

14. J. J. COGLIATI AND A. M. OUGOUAG, "Pebble bed reactor dust production model," 2009, (2009).

15. J. J. COGLIATI, A. M. OUGOUAG AND J. ORTENSI, "Survey of dust production in pebble bed reactor cores," *Nuclear Engineering and Design.* 241, 6, 2364-2369, (2011).

16. X. SHENG, S. YU, X. LUO AND S. HE, "Wear behavior of graphite studies in an air-conditioned environment," *Nuclear Engineering and Design.* 223, 2, 109-115, (2003).

17. Y.-H. TUNG, R. W. JOHNSON AND H. SATO, "Effects of graphite surface roughness on bypass flow computations for an HTGR," *Nuclear Engineering and Design.* 252, 0, 78-87, (2012).

18. L. XIAOWEI, Y. SUYUAN, S. XUANYU AND H. SHUYAN, "The influence of roughness on tribological properties of nuclear grade graphite," *Journal of Nuclear Materials.* 350, 1, 74-82, (2006).

19. X. LUO, X. LI AND S. YU, "Nuclear graphite friction properties and the influence of friction properties on the pebble bed," *Nuclear Engineering and Design.* 240, 10, 2674-2681, (2010).

20. X. Y. SHENG, S. Y. YU, X. W. LUO, S. Y. HE AND Z. S. ZHANG, "Friction surface analysis on Chinese graphite used in nuclear reactor," *Hedongli Gongcheng/Nuclear Power Engineering.* 22, 5, 401-405+455, (2001).

21. X. LUO, S. YU, X. SHENG AND S. HE, "Temperature effect on IG-11 graphite wear performance," *Nuclear Engineering and Design.* 235, 21, 2261-2274, (2005).

22. M. HIRUTA, G. JOHNSON, M. ROSTAMIAN, G. P. POTIRNICHE, A. M. OUGOUAG, M. BERTINO, L. FRANZEL AND A. TOKUHIRO, "Computational and experimental prediction of dust production in pebble bed reactors, Part II," *Nuclear Engineering and Design.* 263, 509-514, (2013).

23. R. S. TROY, R. V. TOMPSON, T. K. GHOSH AND S. K. LOYALKA, "Generation of graphite particles by rotational/spinning abrasion and their characterization," *Nuclear Technology.* 178, 3, 241-257, (2012).

24. J. K. LANCASTER AND J. R. PRITCHARD, "On the 'dusting' wear regime of graphite sliding against carbon," *Journal of Physics D: Applied Physics.* 13, 8, 1551-1564, (1980).

25. J. K. LANCASTER AND J. R. PRITCHARD, "The influence of environment and pressure on the transition to dusting wear of graphite," *Journal of Physics D: Applied Physics.* 14, 4, 747-762, (1981).

26. J. FACHINGER, A. KUMMER, G. CASPARY, M. SEUBERT, A. KOSTER, M. MAKUMBE AND L. NAICKER, "Examination of dust in AVR pipe components," *2008 Proceedings of the 4th International Topical Meeting on High Temperature Reactor Technology, HTR 2008*, 2009, (2009).

27. H. GOTTAUT AND K. KRÜGER, "Results of experiments at the AVR reactor," *Nuclear Engineering and Design.* 121, 2, 143-153, (1990).

28. E. HOINKIS, H. BEHRET, D. HARTMANN, A. KÖHLING AND E. ROBENS, "The corrosion induced change of pore size distribution and surface area of a fuel element graphite," *Thermochimica Acta.* 29, 2, 345-348, (1979).

29. H. ZAÏDI, D. PAULMIER AND J. LEPAGE, "The influence of the environment on the friction and wear of graphitic carbons. II. Gas coverage of wear debris," *Applied Surface Science.* 44, 3, 221-233, (1990).

30. A. LONDONO-HURTADO, I. SZLUFARSKA, R. BRATTON AND D. MORGAN, "A review of fission product sorption in carbon structures," *Journal of Nuclear Materials.* 426, 1-3, 254-267, (2012).

31. B. BHUSHAN, "Modern Tribology Handbook," *CRC Press*, (2000).

32. Z. P. CHEN, X. W. LUO AND S. Y. YU, "Effect of feeding velocity on wear behavior of graphite ball under elevating process with HTGR fuel handling system," *Yuanzineng Kexue Jishu/Atomic Energy Science and Technology.* 46, SUPPL.2, 853-858, (2012).

33. J. D. CHEN AND C. P. JU, "Effect of sliding speed on the tribological behavior of a PAN-pitch carbon-carbon composite," *Materials Chemistry & Physics.* 39, 3, 174-179, (1995).

34. R. N. MORRIS et al., "TRISO-Coated Particle Fuel Phenomenon Identification and Ranking Tables (PIRTs) for Fission Product Transport due to Manufacturing, Operations, and Accidents," *NUREG/CR-6844*, Vol. 3, U.S. Nuclear Regulatory Commission (2004).

35. R. S. TROY, R. V. TOMPSON, T. K. GHOSH AND S. K. LOYALKA, "Generation of Graphite Particles by Sliding Abrasion and their Characterization," *Nuclear Technology.* Accepted 2014, (2014).

36. K. V. E. AL., "Fuel Performance and Fission Product Behavior in Gas Cooled Reactors," *International Atomic Energy Agency.* IAEA-Techdoc- 978, (1997).

CHAPTER 4. CONCLUSIONS

Between these two studies, two different graphites were used and two methods of dust production were explored. The results from these two studies shed light on how dust is produced during PBR operation and the data can be used for many purposes, mainly licensing and operation. Different dust production methods produce different size distributions, wear rates and surface areas but there are common trends across all tests and graphite types.

The common trends throughout both studies are as follows. Loading and rotational/sliding speed have an effect on size distributions, surface roughness, surface areas, particle shapes and wear rates. In general, as the loading or rotational/sliding speed increased so did the concentrations of the dust, surface area of the dust, and wear rate. In all the images of particles produced none were spherical in shape. They all had a jagged irregular shape that would be difficult to predict and didn't seem to follow a pattern. This will need to be taken into account for models that use this information in the future. In general, nuclear grade graphite has a higher concentration of particles produced, wear rate and surface area in comparison to commercial grade graphite.

One significant take away from this study is the increased surface area of the particles. This has large implications in radiation transport as a high surface area will enhance radiation transport throughout the reactor while it is operating as well as in accident scenarios. Not only were there increases but they were large increase sometimes on the order of 100 times more. In addition, this could indicate that the dust is highly reactive and more studies should be performed investigating the interaction of this high

surface area dust and other materials in the reactor, fission products, and other radioactive materials in the reactor in operation as well as accident scenario.

Another important take away from this study is the dust production changes as particles travel through the reactor. This is regardless of the type of wear (sliding or spinning) or the type of graphite (commercial or nuclear grade). Dust production will generally increase as the particle gets to the bottom of the reactor where the loadings are highest. Further investigation needs to be performed on a dynamic load which would more closely mimic a pebble traversing the reactor while operating. When a pebble is going through the reactor we believe that it will experience sliding abrasion, spinning abrasion and both types simultaneously. It seems that sliding abrasion produced higher particle concentrations but if you compare per interaction wear rate spinning abrasion has a higher wear rate indicating a higher particle production per interaction. With the sliding abrasion, there were three points of contact producing particles and with the spinning two points of contact producing particles. It is necessary to keep the different contact points in mind. In addition, different graphites produced different size distributions, with the nuclear grade having higher concentrations under the same conditions.

One piece of data that should not be overlooked is the statistical fits performed on the size distributions. This data can aid models in the future achieve more accurate results. By knowing an equation for the size distribution of the dust, many studies and models should be constructed using this data to determine desired quantities. In addition, statistical analysis can be performed to get desirable quantities such as mean, mode, median, standard deviation and other descriptive statistics about the dust.

VITA

Raymond Troy was born in Bensenville, IL on September 4th 1983. He attended public schools in the Bensenville school district and graduated from Fenton High School in 2002. In 2002, he moved to Columbia, Missouri and studied Mechanical Engineering at the University of Missouri. He graduated with a Bachelor of Science in December of 2006. The first 8 semesters of Raymond's' undergraduate studies were fully financed by the Chick Evan's Scholarship. He went on to further his education achieving a Master of Science from the University of Missouri in Nuclear Engineering in May of 2011. His master's thesis was focused on particle generation from pebble bed reactors. The culmination of his education was finished at the University of Missouri in 2014 with a PhD in Nuclear Engineering.

During his time in Columbia, Raymond became very interested and involved with the community and entrepreneurship. He has volunteered at the Columbia Meals on Wheels for 8 years and served on its board of directors for 6 years. He also served on the Columbia's Better Business Bureau advisory board from 2012 to 2013. Raymond was named Columbia's "30 Under 30" by Vox Magazine in 2011. He founded several businesses and helped start the Allen Angel Capital Education fund at the University of Missouri. He filed his first patent application in 2012 and his second in 2014.